THE ROLE OF SCHLEMM'S CANAL IN AQUEOUS OUTFLOW FROM THE HUMAN EYE

by

Mark Johnson

B.S., Purdue University
(1975)

SUBMITTED IN PARTIAL FULFILLMENT
OF THE REQUIREMENTS FOR THE
DEGREE OF

MASTER OF SCIENCE

at the

MASSACHUSETTS INSTITUTE OF TECHNOLOGY

June, 1981

Signature of Author. . . . . .
Department of Mechanical Engineering, April 24, 1981

Certified by . . . . . .
Thesis Supervisor

Accepted by. . . . . .
Chairman, Department Committee on Graduate Students

THE ROLE OF SCHLEMM'S CANAL IN AQUEOUS OUTFLOW FROM THE HUMAN EYE

by

MARK JOHNSON

Submitted to the Department of Mechanical Engineering
on April 24, 1981 in partial fulfillment of the
requirements for the Degree of
Master of Science.

ABSTRACT

As aqueous humor passes through the outflow network in the human eye, its fluid pressure drops 7 mm Hg in the normal eye and as much as 40 mm Hg in glaucomatous eyes. This study investigates the role of Schlemm's canal in producing this pressure drop.

A mathematical model of Schlemm's canal is constructed in which Schlemm's canal is modeled as a porous, compliant channel which is held open by the trabecular meshwork. The trabecular meshwork is modeled as a series of linear springs which allow the inner wall of Schlemm's canal to deform in proportion to the local pressure drop across it.

We are in the process of obtaining detailed pressure-flow measurements on enucleated human eyes, and the preliminary data is compared with the theoretical model. Based on this comparison and on results reported in the literature, the following tentative conclusions are reached:

(1) Most of the pressure drop in the aqueous outflow network occurs in the inner wall of Schlemm's canal.

(2) Significant collapse of Schlemm's canal only occurs when the intraocular pressure is substantially elevated.

(3) The assumption that the inner wall resistance occurs in pores which are 10 μm in length and 1.5 μm in diameter leads to the conclusion that there are approximately 1400 of the pores in the eye.

(4) Glaucoma is *not* caused by a weakening of the trabecular meshwork and a resultant collapse of Schlemm's canal alone. Glaucoma is likely caused by a decreased porosity of Schlemm's canal inner wall.

Thesis Supervisors:

Roger Kamm
Assistant Professor of
Mechanical Engineering

Ascher H. Shapiro
Institute Professor

ACKNOWLEDGEMENTS

First and foremost my deepest thanks to Professor Roger Kamm whose friendship and guidance was invaluable. I feel quite fortunate to have had him as my advisor. I thank Professor Ascher Shapiro who watched carefully over my work and kept me from going astray.

I am indebted to the staff of the Howe Laboratory and I extend my special thanks to Ms. Joann Lindenmeyer. Without their help and advise this project would not have been possible. My thanks to Dr. P. John Anderson for the use of his perfusion apparatus.

I acknowledge use of the M.I.T. computer language MACSYMA which led to substantial time savings.

Finally, I am indebted to the National Institute of Health (Grant No. 1 R01 EY 03141-01), which provided the financial support of this project.

TABLE OF CONTENTS

Page

NOMENCLATURE

Symbol	Meaning
b	Viscoelastic coefficient of the eye
C	Compliance of the eye, $C \equiv dV/dIOP$
E, E_{TM}	Spring modulus of the trabecular meshwork
E_s	Spring modulus of the septae
E_{eff}	Effective spring modulus which includes the meshwork and septae moduli
$h(x)$	Height of the channel
h_o	Undeformed height of the channel
h_s	Effective height of the septae
h_{eff}	Effective undeformed height of the channel including effects of the meshwork and the septae
$H(x')$	Non-dimensional height of the channel, $H(x') \equiv h(x)/h_o$
IOP	Intraocular pressure
L	Length of "pores" through the juxtacanalicular meshwork
$P(x)$	Pressure within the channel
$\bar{P}(x')$	Non-dimensional pressure within the channel, $\bar{P}(x') \equiv [IOP - P(x')]/E$
P_{cc}	Collector channel pressure
P_v	Episcleral venous pressure
ΔP	Pressure drop $(IOP - P_v)$
$Q(x)$	Volumetric flowrate within the channel
$\bar{Q}(x')$	Non-dimensional flowrate within the channel, $\bar{Q}(x') \equiv \frac{\mu Q(x')s}{wh^3(x')E}$
$\bar{Q}$	Total non-dimensional flowrate through the channel, $\bar{Q} \equiv \bar{Q}(1)$

$\bar{Q}_c(x')$	Non-dimensional flowrate within the compliant section of the channel
$\bar{Q}_c$	Total non-dimensional flowrate through the compliant section of the channel, $\bar{Q}_c = \bar{Q}_c(1)$
$\bar{Q}_R(x')$	Non-dimensional flowrate within the rigid section of the channel
$\bar{Q}_R$	Total non-dimensional flowrate through the rigid section of the channel, $\bar{Q}_R \equiv \bar{Q}_R(1)$
$\bar{Q}'$	Total non-dimensional flowrate through the channel in Regime III of the compliant septae model, $Q = \frac{\mu Q(1)s}{Wh_{eff}^3(1)E_{eff}}$
Q_{in}	Flowrate into the eye
Q_{out}	Flowrate out of the eye
R_{in}	Resistance to flow into the eye (mm Hg·min/μL)
R_{out}	Resistance to outflow from the eye (mm Hg·min/μL)
R_w	Resistance per unit length to flow through the inner wall
$R_{inner\ wall}$	Total resistance to flow through the inner wall
$R_{channel}$	Total resistance to flow caused by the channel
r	Radius of the "pores" through the juxtacanalicular meshwork
s	Length of the channel
S_R	Length of the rigid channel
t	Time
V	Volume of the eye
V_o	Unstressed volume of the eye
W	Width of the channel perpendicular to the paper

x — Axial distance

x' — Non-dimensional axial distance

x_c — Non-dimensional location at which the septae first inhibit Schlemm's canal from further collapse

Greek

α — Ratio of the channel resistance to the inner wall resistance

β — Square root of the ratio of the undeformed channel resistance to the undeformed inner wall resistance,

$$\beta^2 = \frac{12\mu s/Wh_o^3}{R_w/S}$$

β_c — β for the compliant section of the channel

β_R — β for the rigid section of the channel

β' — β for the channel in Regime III of the compliant septae model,

$$\beta'^2 = \frac{12\mu s/Wh_{eff}^3}{R_w/s}$$

ε — Non-dimensional pressure drop, $\varepsilon = \Delta P/E$

ε_c — Non-dimensional pressure drop at which the septae first inhibit further collapse of Schlemm's canal

ε_R — Non-dimensional pressure drop at which the entire canal is collapsed to the septae height

ε' — ε for the channel in Regime III of the compliant septae model, $\varepsilon' = \Delta P/E_{eff}$

τ_Q — Time constant for a constant inflow perfusion experiment

τ_p — Time constant for a constant supply pressure perfusion experiment

μ — Viscosity

CHAPTER I

THE PROBLEM

Open-angle glaucoma is a disease caused by ocular hypertension which results from an obstruction to the outflow of aqueous humor from the eye. Aqueous humor flows through the outflow network at an extremely low flowrate (2.0 μL/min), yet its pressure drop in the glaucomatous eye can be quite dramatic: as much as 40 mm Hg. Suprisingly, the pressure drop of aqueous humor flowing through the outflow network of a normal eye is also quite significant (around 7 mm Hg).

In order to achieve a better understanding of the outflow network, changes in which can lead to ocular hypertension and glaucoma, in this investigation we study the role of Schlemm's canal in producing a pressure drop in the normal eye.

1.1 The Aqueous Humor Circulatory Pathway (Figure 1)

1.1.1 Aqueous inflow. Aqueous humor is formed from blood by a combination of secretion and ultrafiltration in the ciliary processes behind the iris. The rate of formation is nearly constant at 2.0 μL/min, although a rise in the intraocular pressure can decrease the formation rate slightly.

Aqueous humor has fluid properties like those of blood plasma: it has a viscosity 2.5 - 4.0% higher than

water (Moses, 1970), and seems to be isotonic with blood plasma in spite of having a lower concentration of large proteins.

Aqueous, after being formed in the ciliary processes, flows into the posterior chamber. It then proceeds in front of the lens and through the pupil. Once in the anterior chamber, the aqueous flows radially outward toward the angle between the iris and the cornea. Calculations have indicated that there is virtually no pressure drop as the aqueous flows from the ciliary processes to the iridocorneal angle (Friedland, 1978). From the angle, the aqueous flows into the aqueous outflow network.

1.1.2 Aqueous outflow. The aqueous outflow network consists of the trabecular meshwork, Schlemm's canal and the aqueous veins. Figure 2 shows the trabecular meshwork and Schlemm's canal.

The trabecular meshwork can be thought of as a series of porous sheets through which the aqueous humor percolates on its way to Schlemm's canal. It can be considered to consist of three layers: The corneoscleral meshwork, the juxtacanalicular meshwork, and the endothelial lining of Schlemm's canal.

The corneoscleral meshwork (Tripathy, 1974) consists of 8 to 15 flattened, perforated sheets of mean thickness 3μm which are connected by trabecular beams. The spaces in the corneoscleral meshwork can be divided into two classes: the inter-trabecular spaces -- spaces between

adjacent sheets varying in size from 0 to 8 μm; and, the intratrabecular spaces -- spaces formed by the perforations in the trabecular sheets varying from 25 to 75 μm in diameter near the angle, and decreasing to from 2 to 15 μm in diameter in the deeper levels of the corneoscleral meshwork. The intra-trabecular spaces do not superimpose in succeeding layers, and thus the aqueous humor travels a tortuous path as it traverses this filter-like tissue.

The mechanism by which aqueous humor passes through the juxtacanalicular meshwork and the endothelial lining of Schlemm's canal is imprecisely known. There are currently three theories:

(i) Tripathy (1971) has proposed that giant vacuoles observed in the endothelial lining of Schlemm's canal may transport fluid by passive macropinocytosis.

(ii) Bill (1972) has observed pores in the endothelial lining, but there is a question as to whether they are artifacts of the fixation process (Johnstone, personal communication).

(iii) Johnstone (1974) has demonstrated endothelial tubules in Schlemm's canal, but it is not yet certain that they have a role in fluid transport; they may only have a structural role.

To avoid the complexities of these various models, this study assumes the juxtacanalicular meshwork and endothelial lining to have a flow resistance per unit

of face area which is independent of the local pressure drop across it. The mechanism responsible for this flow resistance will be an important area for future research.

Upon passing through the endothelial lining, the aqueous enters Schlemm's canal which has the appearance of a highly elongated ellipse in cross-section, measuring 250 μm by from 2 to 30 μm. The inner wall (viewed from within the canal) is a surface dominated by the giant vacuoles of the endothelial lining which invade the canal. The outer wall has no distinguishing characteristics except for the occasional opening that leads to the collector channels. The canal is occasionally interrupted by a septum (or endothelial tubule) which connects the inner wall with the outer wall (as if it were a beam). They are especially numerous near collector channels suggesting that they may serve to prevent occlusion of the collector channels.

After the aqueous humor enters the canal, it travels circumferentially around the canal until it reaches one of the openings which lead to the collector channels. The collector channels connect Schlemm's canal with the aqueous veins.

The aqueous veins carry the aqueous humor to the surface of the eye where they anastomose with the episcleral veins. The aqueous veins are 10 - 100 μm in radius, and despite numerous casting studies their path through the sclera is still not well known.

1.2 The Physiological Significance of the Aqueous Humor Circulatory System

1.2.1 The function of aqueous humor. The eye is a unique biological structure which must provide a transparent path by which light can reach the retina, while also providing for the normal biological needs of the eye tissue. Blood is not transparent, and therefore cannot provide for the biological needs of the tissue in the optical pathway (the lens and the cornea). Aqueous humor can satisfy these needs since it is clear and yet can carry oxygen and nutrients.

1.2.2 The function of the trabecular meshwork and Schlemm's canal. These structures appear to serve three important fuctions:

(i) Act as a barrier to the reflux of blood through the aqueous outflow network into the eye so that red blood cells do not enter the visual field.

(ii) Prevent debris (e.g. pigment), which will tend to flow along with the aqueous into the trabecular meshwork, from accumulating in the juxtacanalicular meshwork.

(iii) Maintain intraocular pressure which provides ocular rigidity which is necessary for visual clarity.

The most effective barrier to reflux through the aqueous outflow network would be an active transport system, or a filter with extremely small opening ($\sim 1000^{o}$). However,

both of these possibilities would preclude removal of debris from the eye. Similarly, a system with large openings to facilitate the removal of debris would be unsuitable as a blood-aqueous barrier. Thus functions (i) and (ii) appear to be contradictory.

The trabecular meshwork is a compromise system which serves both functions. It also serves to maintain the intraocular pressure.

(i) Barrier to blood reflux. The retrograde flow of venous blood is normally prevented by the higher hydrostatic pressure in the aqueous veins. A rise in venous blood pressure will increase the intraocular pressure due to engorgement of the intraocular veins, and thus is not likely to reverse this pressure gradient. However, if the intraocular pressure does not increase as much as the central venous pressure, or if the episcleral venous pressure alone is increased by local occlusion, blood can reflux into the aqueous veins which lead to Schlemm's canal.

The endothelial lining of Schlemm's canal is the first line of defense against the red blood cells. It has openings the maximum diameter of which is thought to be around two microns. (Huggert, 1955). These openings inhibit the reflux of red blood cells into the eye. These small openings continue into the juxtacanalicular meshwork where they further impede red blood cell reflux.

The final barrier to this reflux is the one-way valve

action of the trabecular meshwork. The meshwork acts like a sponge which is bound circumferentially at the angle. As the intraocular pressure increases, the sponge expands; when venous pressure increases, the sponge closes down. In this way, the meshwork acts as a one-way valve which closes down when venous pressure increases relative to the intraocular pressure. (Johnstone and Grant, 1973). It can be noted here that this one-way action is directly a result of the existence of Schlemm's canal and the meshwork tethering at the angle. Without the canal, the trabecular meshwork would be attached to the corneoscleral wall, and would be unable to close down in response to a change in venous pressure.

(ii) Removal of the debris. Any inflammatory response in the eye can result in debris which needs to be removed from the eye. If this debris were to flow unimpeded with the aqueous humor, it would plug up the juxtacanalicular meshwork. Therefore the corneoscleral meshwork acts as a filter to trap the material before it gets to the juxta-canalicular meshwork. Once trapped, it is engulfed by trabecular endothelial cells acting as stationary macrophages (Richardson, Hutchinson and Grant, 1977).

Once the material has been digested, the endothelial cells release themselves from the trabecular wall and flow out with the aqueous humor. The corneoscleral meshwork offers almost no resistance when the intraocular pressure is greater than venous pressure. The cells are ameboid and are therefore able to slide through the juxtacanalicular meshwork.

(iii) Maintenance of the intraocular pressure. The small openings in the juxtacanalicular meshwork and the endothelial lining of Schlemm's canal are well suited to provide considerable fluid resistance and thus maintain the intraocular pressure.

1.3 The Principal Site of Flow Resistance

In view of the extremely slow rate of aqueous humor flow through the outflow network (2.0 μL/min) and the short flow distance (less than one millimeter), the pressure drop is suprisingly large (7 mm Hg). Many studies have sought to determine the principal site of resistance. Toward this end, a number of pressure - flow curves have been determined experimentally. Qualitatively these studies indicate that the relationship between pressure and flow is nearly linear with the flow resistance increasing slowly with pressure.

A number of sites have been identified as possible sources of this resistance:

(i) corneoscleral meshwork

(ii) juxtacanalicular meshwork

(iii) endothelial lining of the inner wall of Schlemm's canal

(iv) Schlemm's canal

(v) aqueous veins

1.3.1 The corneoscleral meshwork. Two considerations preclude the corneoscleral meshwork from being the principle site of resistance: (1) the size of the openings in the

trabecular meshwork is too large to cause an appreciable resistance. (2) Johnstone and Grant (1973) showed that as the intraocular pressure increases, the trabecular meshwork opens up like a sponge bound where the flow enters (See Figure 3). If the corneoscleral meshwork were the principal site of resistance, then one would expect the flow resistance to decrease as the intraocular pressure increases. However, experiments on human eyes have shown that this is not the case.

1.3.2 The inner wall: the juxtacanalicular meshwork and the endothelial lining of Schlemm's canal. Because the precise mechanism by which aqueous humor passes through this region is not well known, this region is considered as the inner wall of Schlemm's canal in this study.

There is good reason to believe that this region is the principal site of resistance. Perfusion studies with tracers used to determine the smallest flow dimensions in the outflow network have consistently shown the inner wall to have the smallest flow dimensions (Huggert, 1955). These flow dimensions are estimated at 1.5 μm in diameter which is consistent with the observed pressure drop.

Another compelling reason to consider the inner wall to be the principal site of resistance is found in the work done by Bill and Svedbergh (1972, 1980). They estimated the number of pores in the endothelial lining of Schlemm's canal, and found that there were too many pores to account for the known resistance. However, when they added Na_2EDTA

(a chelating agent which binds calcium and thereby disrupts cell junctions) to the aqueous outflow pathway, they found the juxtacanalicular region and the endothelial lining generally disrupted; and, the number of pores they observed accounted for the measured flow resistance.

This suggests that the juxtacanalicular meshwork is the primary site of resistance, and Na_2EDTA dramatically decreases this resistance by opening up this region.

1.3.3 Schlemm's canal. Two characteristics of Schlemm's canal make it particularly well-suited to contribute to flow resistance in the outflow network: (1) As the trabecular meshwork expands in response to increasing intraocular pressure, Schlemm's canal is narrowed. It has the potential to collapse to an extremely narrow channel which would generate considerable flow resistance. (2) Schlemm's canal narrows with increasing intraocular pressure which is consistent with experiments showing increased flow resistance with increased intraocular pressure.

1.3.4 Aqueous veins. The diameter of the aqueous veins is much too large to cause any appreciable resistance (Battaglioli, 1981). Stresses in the sclera due to the intraocular pressure could conceivably cause collapse of the aqueous veins (and thus generate significant flow resistance), but recent work shows that this does not occur until the intraocular pressure is substantially elevated (Battaglioli, 1981).

1.4 Our Approach to the Problem

It appears likely that the principal site of flow resistance is either the inner wall of Schlemm's canal, or Schlemm's canal or both. In this study, therefore, we investigate a theoretical model which accounts for the flow resistance of both. Experimental pressure-flow curves obtained from enucleated human eyes are then compared with the theoretical model.

CHAPTER II

A MODEL OF SCHLEMM'S CANAL AS A POROUS, COMPLIANT CHANNEL

The flow model is two-dimensional (Figure 4). Aqueous humor flows from the trabecular meshwork (T.M.) through the inner wall, which is assumed to have constant flow resistance per unit of face area, into Schlemm's canal. The flow through Schlemm's canal is modeled as a two-dimensional, quasi-rectilinear, inertia-free flow between two nearly parallel sheets. The lower sheet represents the flexible inner wall of Schlemm's canal, the structual support of which is provided by the meshwork attachment. In the model, the attachment is represented by linear springs which allow the inner wall to deform in proportion to the local pressure drop across it. The upper sheet, assumed rigid, represents the outer wall. After entering the canal, the fluid travels circumferentially until it reaches one of the collector channels. There are assumed to be 30 of these equally spaced every 1200 μm around the circumference of the eye.

2.1 The Theory of Viscous Flow Through a Porous, Compliant Channel

The problem of viscous flow through various types of channels has numerous applications in physiology. Fung (1977) analyzed the viscous flow of blood between the compliant alveolar sheets in the lungs. Kenyon (1980) modeled the flow

of synovial fluid through cartilage in joints as viscous flow through a porous channel. Here we consider the general case of viscous flow through a porous, compliant channel.

2.1.1 The derivation of the governing differential equation. The geometry of the system is shown in Figure 4. The fluid pressure is assumed constant until it flows through the inner wall. For the aqueous outflow network this pressure is the intraocular pressure (IOP). The inner wall is assumed to have a constant resistance (R_w) per unit length along the channel. Using the continuity equation, these two assumptions are combined to yield a relationship between flowrate ($Q(x)$) and pressure ($P(x)$) at a location in the channel.

$$\frac{dQ(x)}{dx} = \frac{[IOP - P(x)]}{R_w} \qquad (2.1)$$

Because the channel height ($h(x)$) is assumed to vary slowly with position and is typically much smaller than the width of the channel, the flow is modeled as quasi-rectilinear flow between two nearly parallel sheets. The Reynolds number of the flow is much less than one and hence the flow is inertia-free. The well-known solution of the Navier-Stokes equations for two-dimensional, inertia-free channel flow is:

$$\frac{dP(x)}{dx} = -\frac{12\mu Q(x)}{Wh^3(x)} \qquad (2.2)$$

where W is the width of the channel perpendicular to the paper

The inner wall is held away from the outer wall by a series of linear springs which allow the inner wall to deform in proportion to the local pressure drop across it. The displacement of these springs is described as follows:

$$\frac{h(x) - h_o}{h_o} = \frac{1}{E}[P(x) - IOP] \qquad (2.3)$$

where E is the modulus of the springs

h_o is the undeformed height of the channel

Although the relationship is here assumed linear, the implications of other non-linear forms will later be addressed.

Two boundary conditions are applied (see Figure 4). (1) By symmetry, there is no flow at the beginning of the channel (x = 0); this corresponds to a point halfway between two collector channels in Schlemm's canal. (2) The pressure at the end of the channel (x=s) is the collector channel pressure (P_{cc}).

$$(1) \quad Q(0) = 0$$

$$(2) \quad P(S) = P_{cc}$$

It is convenient here to introduce several non-dimensional variables.

$$H(x) \equiv \frac{h(x)}{h_o} = 1 - \frac{IOP - P(x)}{E}$$

The non-dimensional height. It varies between zero (totally collapsed) and one (the undeformed state)

$$\varepsilon \equiv \frac{(IOP - P_{cc})}{E}$$

The non-dimensional pressure drop of the system

$$x' \equiv x/s$$

The non-dimensional distance along the channel.

$$\beta^2 \equiv \frac{12\mu s/Wh_o^3}{R_w/s}$$

The ratio between the resistance in the undeformed channel and the resistance of the inner wall.

2.1.2 The governing differential equation. The non-dimensional variables are now introduced, and Equations (2.1) - (2.3) are combined to yield the single governing differential equation:

$$\beta^2\left[H(x') - 1\right] = H^3(x')\frac{d^2H(x')}{dx'^2} + 3H^2(x')\left[\frac{dH(x')}{dx'}\right]^2 \qquad (2.4)$$

The first boundary condition is related to H(x') using Equation (2.2). The non-dimensional boundary conditions are:

$$(1)\quad \frac{dH(0)}{dx'} = 0$$

$$(2)\quad H(1) = 1 - \varepsilon$$

Equation (2.4) indicates that, since the non-dimensional height H(x') varies between zero and one, $d^2H(x')/dx'^2 \leq 0$. With the exception of the trivial case of constant height, we conclude that there are no inflection points in the curve for channel height: the rate of collapse of the channel increases as the collector channel is approached (e.g. Figure 6).

This result can be explained physically as follows. Due to viscosity, the pressure of the fluid drops as it moves through the channel. As the pressure drops, the pressure difference acting across the inner wall increases causing the channel to become narrower. As the channel narrows, the viscous forces increase due to the fluid being forced through a

smaller space. This increases the pressure drop in the channel and accelerates the rate of collapse.*

It can also be noted here the Equation (2.4) has a singularity when the non-dimensional height becomes zero. As the pressure at the exit of the channel is reduced, the flowrate through the channel increases and the height of the channel decreases. The maximum flowrate is reached as height of the channel approaches zero. *However*, when the channel height at the exit becomes zero ($\varepsilon = 1$), the flowrate drops to zero. This is the source of the singularity in Equation (2.4).

This discontinuity would not occur in a physical system. Inertial forces, which have been neglected in this analysis, become important as the height of the channel approaches zero.

2.1.3 Solution of the governing differential equation. Equation (2.4) is an autonomous differential equation. Thus the order of the equation can be reduced by making the autonomous substitution: $U = dH(x')/dx'$. We use this substitution and incorporate the first boundary condition of Equation (2.4).

$$\left[\frac{dH(x')}{dx'}\right]^2 = \frac{2\beta^2}{H^6(x')}\left[\frac{H^5(x')}{5} - \frac{H^4(x')}{4} + \frac{H^4(0)}{4} - \frac{H^5(0)}{5}\right]$$

---

*One might say that it is a viscous circle.

We take the square root of the equation keeping the negative root since the pressure gradient is negative.

$$\frac{dH(x')}{dx'} = -\frac{\sqrt{2}\beta}{H^3(x')}\left[\frac{H^5(x')}{5} - \frac{H^4(x')}{4} + \frac{H^4(0)}{4} - \frac{H^5(0)}{5}\right]^{1/2} \tag{2.5}$$

It is useful here to introduce the non-dimensional flowrate.

$$\bar{Q}(x') \equiv \frac{\mu Q(x')S}{Wh_o^3E}$$

Equation (2.2) is used to relate the non-dimensional flowrate to the non-dimensional channel height

$$\bar{Q}(x') = -\frac{H^3(x')}{12}\frac{dH(x')}{dx'} \tag{2.6}$$

We combine this result with Equation (2.5).

$$\bar{Q}(x') = \frac{\sqrt{2}\beta}{12}\left[\frac{H^5(x')}{5} - \frac{H^4(x')}{4} + \frac{H^4(0)}{4} - \frac{H^5(0)}{5}\right]^{1/2}$$

Finally, the total flowrate through the channel ($\bar{Q}$) is found by evaluating this equation at x' = 1.

$$\bar{Q} \equiv \bar{Q}(1) = \frac{\sqrt{2}\beta}{12}\left[\frac{H^5(1)}{5} - \frac{H^4(1)}{4} + \frac{H^4(0)}{4} - \frac{H^5(0)}{5}\right]^{1/2} \tag{2.7}$$

H(1) is given in the boundary conditions, but H(0) is unknown. It can only be found by solving Equation (2.5). Unfortunately, attempts to solve this equation analytically have been unsuccessful.

2.2 Perturbation Solutions of the Governing Differential Equation

When applying perturbation analysis to Equation (2.4), two possible perturbation parameters are apparent: β^2 and ε.

$$\overline{Q} = \overline{Q}(\beta^2, \varepsilon)$$

ε varies between zero and one; as will be shown later, we have reason to believe that β^2 in the Schlemm's canal system is much less than one. Therefore, it appears natural to pursue a perturbation series in β^2.

2.2.1 Perturbation series in β^2. $H(x')$ is expanded as a perturbation series in β^2.

$$H(x') = H_0(x') + \beta^2 H_1(x') + \beta^4 H_2(x') + O(\beta^6)$$

This series is substituted into Equation (2.4). A series of equations result subject to the boundary conditions:

$$\frac{dH_0(0)}{dx'} = 0 \qquad H_0(1) = 1 - \varepsilon$$

$$\frac{dH_N(0)}{dx'} = 0 \qquad H_N(1) = 0 \qquad N > 0$$

The series of equations which result were both determined and solved by an M.I.T. computer language known as MACSYMA. The use of MACSYMA led to substantial time savings, and allowed the calculation of terms in the perturbation series that would not otherwise have been attempted.

The resulting solutions for the perturbation series is found to be:

$$H(x') = (1-\varepsilon) + \frac{\varepsilon(1-x'^2)\beta^2}{2(1-\varepsilon)^3} + \frac{\varepsilon(1-x'^2)\left[(8\varepsilon+1)x'^2 - 4\varepsilon - 5\right]\beta^4}{24(1-\varepsilon)^7} + O(\beta^6)$$

To find the flowrate through the system, the perturbation series for the non-dimensional height is substituted into Equation (2.6) and evaluated at $x' = 1$.

$$\bar{Q} = \frac{\varepsilon\beta^2}{12} - \frac{\varepsilon\beta^4}{36(1-\varepsilon)^3} + \frac{\varepsilon(\varepsilon+2)\beta^6}{180(1-\varepsilon)^7} - O(\beta^8) \qquad (2.8)$$

For small values of ε and β^2, the relation for $\bar{Q}$ can be approximated:

$$\bar{Q} \sim \varepsilon\beta^2/12 \qquad (2.9)$$

However, as ε approaches one, the asymptotic relation in Equation (2.8) can be seen to be divergent. Other than the linear relationship between flowrate and pressure drop indicated in Equation (2.9), the only additional information that can be gleaned from Equation (2.8) is an evaluation of the extent of validity of Equation (2.9).

For this determination, define the second term of the perturbation series (2.8) to be negligible when it is less than one percent of the first term.

$$\frac{\varepsilon\beta}{12}^2 \geq \frac{100\varepsilon\beta^4}{36(1-\varepsilon)}^3$$

Therefore, the linear approximation in Equation (2.9) is valid for:

$$\varepsilon < 1 - 3.22\beta^{2/3}$$

That is, for small β *and* no more than moderate degrees of collapse.

Physically Equation (2.9) says that all of the pressure drop occurs in the inner wall, which is what one would expect for small β^2.

2.2.2 Perturbation series in ε. It is also useful to pursue a perturbation solution for H(x') in terms of a series in ε which is again expected to be valid only for moderate collapse.

$$H(x') = H_0(x') + \varepsilon H_1(x') + \varepsilon^2 H_2(x') + O(\varepsilon^3)$$

This series is substituted into Equation (2.4). A series of equations result subject to the boundary conditions:

$$\frac{dH_0(0)}{dx'} = 0 \qquad H_0(1) = 1$$

$$\frac{dH_1(0)}{dx'} = 0 \qquad H_1(1) = -1$$

$$\frac{dH_N(0)}{dx'} = 0 \qquad H_N(1) = 0 \qquad N > 1$$

MACSYMA was once again used to determine and solve the resultant equations.

$$H(x') = 1 - \frac{\cosh(\beta x')\varepsilon}{\cosh \beta} + \frac{\cosh(2\beta)}{\cosh^2\beta}\left[\frac{\cosh(\beta x')}{\cosh \beta} - \frac{\cosh(2\beta x')}{\cosh(2\beta)}\right]\varepsilon^2 - O(\varepsilon^3)$$

The perturbation series for non-dimensional height is substituted into Equation (2.6) and evaluated at $x' = 1$.

$$\bar{Q} = \left[\frac{\beta \tanh \beta}{12}\right] \varepsilon + O(\varepsilon^2) \qquad (2.10)$$

Equation (2.10) is interesting in that the first term of the perturbation series is the solution for the flowrate through a rigid channel with a porous wall (Moses, 1979). Equation (2.9) is the small β^2 approximation to Equation (2.10).

As discussed in Section 2.1.2, Equation (2.4) has a singularity at $\varepsilon = 1$. This singularity is the source of the divergent nature of the perturbation series and limits their usefulness to the linear segment of the pressure-flow curve.

For further progress on the solution to the governing differential equation, a numerical approximation is needed.

2.3 Numerical Solution of the Governing Differential Equation

Two different numerical methods are available for solving Equation (2.4): One could use the standard differential equation solvers such as Runge-Kutta, or one could numerically integrate Equation (2.5) which is the first integral of

Equation (2.4). "Numerical integration, in contrast to differentiation, is basically a stable process" (Conte and deBoor, 1965). Therefore, Equation (2.5) is integrated.

Begin by defining g(H):

$$g(H) \equiv -\frac{\sqrt{2}\beta}{H^3}\left[\frac{H^5}{5} - \frac{H^4}{4} + \frac{H^4(0)}{4} - \frac{H^5(0)}{5}\right]^{1/2}$$

Equation (2.5) then becomes:

$$H(x') - H(1) = \int_1^{x'} g\left[H(x')\right](-dx') \qquad (2.11)$$

The numerical integration starts at $x' = 1$ because this is where the boundary condition on $H(x')$ is given. The independent variable is discretized in a manner consistent with the integration beginning at $x' = 1$ and proceeding toward $x' = 0$.

$$N\Delta x = 1 - x'$$

where Δx is the step size

N is the step number

The boundary condition at $x' = 0$ has already been satisfied in deriving Equation (2.5), but the constant $H(0)$ is still an unknown which is necessary to evaluate $g(H)$. The boundary condition at $x' = 1$ uniquely determines $H(0)$, although the value of $H(0)$ is a result of the numerical integration. Determination of $H(0)$ therefore must be accomplished in an iterative fashion.

The bisection method (Conte and deBoor, 1965) is used to guess successive values of $H(0)$. The initial bounds on the bisection are $H(1)$ and one. The value guessed for $H(0)$ is

used in the numerical integration of Equation (2.11). When the value guessed is sufficiently close to the value obtained from the numerical integration of Equation (2.11), the iteration ends.

2.3.1 The numerical integration. For N = 0, the solution for H(x')(=H(1)) is given in the boundary conditions. For N=1, a Taylor series approximation for H(x') is used.

$$H(1-\Delta x) = H(1) - \frac{dH(1)}{dx'}\Delta x + \frac{d^2H(1)}{dx'^2}\Delta x^2 + O(\Delta x^3)$$

where:

$$\frac{dH(1)}{dx'} = -\frac{\sqrt{2}\beta}{H^3(1)}\left[\frac{H^5(1)}{5} - \frac{H^4(1)}{4} + \frac{H^4(0)}{4} - \frac{H^5(0)}{5}\right]^{1/2}$$

$$\frac{d^2H(1)}{dx'^2} = \frac{\beta^2}{H^3(1)}\left[H(1) - 1\right] - \frac{3}{H(1)}\left[\frac{dH(1)}{dx'}\right]^2$$

The equations for the first and second derivatives are Equations (2.4) and (2.5) evaluated at x' = 1.

For N = 2 and all higher even-numbered steps, Simpson's rule is used. For convenience of notation H(1 - NΔx) is represented as H_N.

$$H_N - H_0 = -\frac{\Delta x}{3}\Big[g(H_0) + 4g(H_1) + 2g(H_2) + 4g(H_3) + 2g(H_4) + \ldots + 4g(H_{N-1}) + g(H_N)\Big] + O(\Delta x^4) \qquad (2.12)$$

Note that in Equation (2.12), H_N is required on the right hand side of the equation. Since this is what is being

solved for, its value is estimated. This is done using a Taylor series.

$$H_N = H_{N-1} - \frac{dH_{N-1}}{dx'} \Delta x + O(\Delta x^2)$$

The first derivative required for this expression is estimated using a 3-point backward differencing scheme.

$$\frac{dH_{N-1}}{dx'} = -\left[\frac{3H_{N-1} - 4H_{N-2} + H_{N-3}}{2\Delta x}\right] + O(\Delta x^2)$$

When the Taylor series is substituted into the right hand side of Equation (2.12), the order of the error is reduced to third order.

For odd-numbered steps a small change is necessary, since the ordinary Simpson's rule does not end on odd-numbered steps. For odd-numbered steps, the ordinary Simpson's rule will be used to find H_{N-3}. Then the Simpson's 3/8 rule will be used to calculate H_N.

$$H_N - H_{N-3} = -\frac{3\Delta x}{8}\left[g(H_{N-3}) + 3g(H_{N-2}) + 3g(H_{N-1}) + g(H_N)\right] + O(\Delta x^n) \qquad n > 4 \tag{2.13}$$

As with Equation (2.12), it is once again necessary to estimate H_N using a Taylor series. The same formulation is used.

One thousand steps were used to divide up the interval between x' = 1 and x' = 0. The integration stops at step number 999. The boundary condition at x' = 0 indicates that

$H_{999} = H_{1000}$. If the value obtained for H_{1000} is sufficiently close to the guess for H(0), the iteration stops (the criterion for convergence is $[H(0) - H_{1000}] \leq 3 \times 10^{-7}$). If the value is not yet converged, the bisection method is used to make a new guess for H(0).

The computer program used is listed in appendix A. It calculates H(x') and $\overline{Q}$. $\overline{Q}$ (the non-dimensional flowrate) is calculated using Equation (2.7).

2.3.2 Results from the numerical solution. It is useful in evaluating the numerical results to define what is meant by the resistance of the inner wall and the resistance of the channel (Schlemm's canal). The continuity Equation (2.1) is integrated yielding:

$$Q(S) = \frac{1}{R_w} \int_0^S [IOP - P(x)]dx$$

define:

$$P_{channel} \equiv \frac{1}{S} \int_0^S P(x)dx$$

$$\Delta P \equiv IOP - P_{cc}$$

$$R_{\substack{inner \\ wall}} \equiv R_w/S$$

$$R_{channel} = \frac{\Delta P}{Q(S)} - R_{\substack{inner \\ wall}}$$

These definitions are used to find the ratio of the channel resistance to the inner wall resistance (α).

$$\alpha \equiv \frac{R_{channel}}{R_{\substack{inner \\ wall}}} = \frac{P_{channel} - P_{cc}}{IOP - P_{channel}} \qquad (2.14)$$

Figures 5, 6 and 7 show the variation of the non-dimensional height with non-dimensional distance along the channel. There is no appreciable pressure drop in the channel for small ε; but as ε increases, the pressure drop in the channel becomes significant with most of it occuring near the exit. As β increases, this effect is amplified.

For small values of β, the resistance of the inner wall is always much greater than that of the channel; however, changes in ε make dramatic changes in the channel resistance.

Figures 8 and 9 show the non-dimensional pressure-flow curves for various values of β. For small β, the curves are linear until the channel is significantly collapsed. The non-linearity increases dramatically in magnitude as β increases. Since the aqueous outflow curves of the human eye show only small non-linearities, one expects that β is small for Schlemm's canal.

The curves stop at $\varepsilon = 0.9$ because of the singularity at $\varepsilon = 1$. Most likely, septae prevent total collapse of Schlemm's canal and this case is considered in the next chapter.

CHAPTER III

A MODEL OF SCHLEMM'S CANAL AS A POROUS, COMPLIANT CHANNEL WITH COMPLETE COLLAPSE PREVENTED BY SEPTAE

The model introduced in Chapter II has a singularity when the channel completely collapses. The singularity, as is discussed Section 2.1.2, occurs at $\epsilon = 1$. It is however unlikely that total collapse of Schlemm's canal actually occurs due to the presence of septae (or endothelial tubules) in Schlemm's canal as have been observed by many investigators (Johnstone, 1974; Hoffman, 1971). These septae are concentrated near collector channels where our model predicts collapse would first occur and where they would therefore be of greatest value. Johnstone (personal communication) has estimated that there are 2000 endothelial tubules in the human eye.

In this chapter, we model the septae as supporting members which inhibit Schlemm's canal from further collapse when the canal has collapsed sufficiently for the supporting members to become effective. The supporting members are assumed to be distributed uniformly along Schlemm's canal. First they are considered to be rigid, and, subsequently, elastic.

3.1 Septae Modeled as Rigid Structures

In this section the septae are modeled as rigid supporting members which prevent the channel from collapsing to a height smaller than the effective height of the supporting members (hereafter, the effective height of the supporting

members is referred to as the post height).

Schlemm's canal is modeled in one of three ways depending on the magnitude of the pressure drop acting across it. For non-dimensional pressure drops below a certain value (ε_C), the channel height is everywhere greater than the post height, and the channel behaves as the porous, compliant channel of Chapter II. For non-dimensional pressure drops greater than a certain value (ε_R), the channel is everywhere collapsed to the height of the posts, and the channel behaves as a porous, rigid channel. For non-dimensional pressure drops between ε_C and ε_R, the part of the channel nearer the collector channel behaves as a porous, rigid channel while the remainder behaves as a porous, compliant channel as shown in Figure 10. We start the analysis of this flow network by studying the flow in a porous, rigid channel.

3.1.1 The theory of viscous flow in a porous, rigid channel. In this section, we consider the general case of viscous flow in a porous, rigid channel; its application to Schlemm's canal is considered in the next section.

The development followed here is similar to that of Section 2.1.1 with two important exceptions: (i) the height of the channel is constant; and (ii) the boundary condition at the beginning of the rigid channel is changed to allow for a non-zero inflow.

Equation (2.1) is still applicable, but Equation (2.2) must be altered to reflect the change in geometry.

$$\frac{dP(x)}{dx} = -\frac{12\mu Q(x)}{Wh_s^3} \qquad (3.1)$$

where h_s is the constant height of the channel (the post height)

The boundary condition at the beginning of the channel ($x = 0$) is expressed using Equation (3.1).

(1) $$\frac{dP(0)}{dx} = -\frac{12\mu Q(0)}{Wh_s^3}$$

The second boundary condition is the same as that for the compliant channel: the pressure at the end of the channel ($x = S_R$) is the collector channel pressure (P_{cc}).

(2) $$P(S_R) = P_{cc}$$

Several changes are necessary in the definition of the non-dimensional variables:

$x' \equiv x/S_R$ — The non-dimensional distance along the rigid channel. S_R is the length of this channel.

$\overline{P}(x') \equiv \frac{IOP - P(x')}{E}$ — The non-dimensional pressure. E is the elastic modulus of the trabecular meshwork defined in Chapter II.

$\overline{Q}_R(x') \equiv \frac{\mu Q(x')S_R}{Wh_s^3 E}$ — The non-dimensional flowrate

$\beta_R^2 \equiv \frac{12\mu S_R/Wh_s^3}{R_W/S_R}$ — The ratio between the resistance in the channel and the resistance in the inner wall

ε, as in Chapter II, is the non-dimensional pressure evaluated at $x' = 1$.

The non-dimensional variables are now introduced, and Equations (2.1) and (3.1) are combined to yield the single differential equation for viscous flow in a porous, rigid channel with a non-zero inflow at $x' = 0$,

$$\frac{d^2\bar{P}(x')}{dx'^2} - \beta_R^2\bar{P}(x') = 0 \tag{3.2}$$

for which the boundary conditions are:

(1) $$\frac{d\bar{P}(0)}{dx'} = 12\bar{Q}_R(0)$$

(2) $$\bar{P}(1) = \varepsilon$$

Equation (3.2) is solved analytically, yielding:

$$\bar{P}(x') = \frac{\varepsilon \mathrm{COSH}(\beta_R x')}{\mathrm{COSH}\ \beta_R} + \frac{12\bar{Q}_R(0)}{\beta_R}\left[e^{-\beta_R}\frac{\mathrm{COSH}(\beta_R x')}{\mathrm{COSH}\ \beta_R} - e^{-\beta_R x'}\right] \tag{3.3}$$

Finally Equation (3.3) is substituted into Equation (3.1) and evaluated at $x' = 1$ to find the total flowrate exiting through the collector channel.

$$\bar{Q}_R = \frac{\varepsilon\beta_R \mathrm{TANH}\beta_R}{12} + \bar{Q}_R(0)e^{-\beta_R}\left[1 + \mathrm{TANH}\beta_R\right] \tag{3.4}$$

Setting $\bar{Q}_R(0) = 0$, this simply reduces to the first order perturbation solution to the compliant wall problem (Equation 2.10).

3.1.2 Combining the rigid channel and the compliant channel solutions. Unlike the situation described in Chapter II for which one solution describes the entire range of pressures, the addition of rigid septae within the channel gives rise to three separate flow regimes (see Figure 11):

Regime I ($\varepsilon<\varepsilon_c$) The channel height is everywhere greater than the post height, and thus the channel behaves as the porous, compliant channel described in Chapter II.

Regime II ($\varepsilon_c<\varepsilon<\varepsilon_R$) Within this range of ε, the channel can be divided into two parts: one, extending from $x'=0$ to $x'=x_c$ where the channel has a height greater than the post height and behaves as the porous, compliant channel of Chapter II; and the other extending from $x'=x_c$ to $x'=1$ where the channel is collapsed to the post height and behaves as the porous, rigid channel described in Section 3.1.1.

Regime III ($\varepsilon>\varepsilon_R$) The channel height is everywhere collapsed to the post height (h_s), constrained from further collapse, and is described in Section 3.1.1.

The pressure-flow characteristics of Regime I are as described in Chapter II; the characteristics of Regime III are as described in Section 3.1.1 with $\bar{Q}_R(0)=0$. The remainder of this section will describe the pressure-flow characteristics of Regime II.

The parameters for the compliant section of the channel are necessarily different than those in the rigid section, since their characteristic dimensions are different. Since these parameters also need definition for the system as a whole, three definitions of each are given in Table I.

The non-dimensional flowrate in the compliant section ($\bar{Q}_C$) is a function of the resistive parameter for that section (β_C) and the non-dimensional pressure at the end of the compliant section (ε_C). The non-dimensional flowrate in the rigid section ($\bar{Q}_R$) is a function of the resistive parameter for that section (β_R), the flowrate entering the rigid section from the compliant section, and the non-dimensional pressure at the exit (ε).

These two coupled solutions determine the pressure-flow characteristics of the system as a whole in Regime II. The procedure used to calculate these parameters is as follows:

(1) Values are chosen for β and ε_C. These are the two parameters which control the pressure-flow characteristics of the system.

(2) The non-dimensional location where the compliant section ends and the rigid section begins ($x_{C)}$ is allowed to vary between zero and one.

(3) The resistive parameter for the compliant section is calculated.

$$\beta_C = x_C \beta$$

(4) The computer program discussed in Chapter II is

used to find the non-dimensional flowrate in the compliant section.

$$\overline{Q}_c(1) = \overline{Q}_c(\beta_c, \varepsilon_c)$$

(5) The flowrate at the end of the compliant section must be equal to the flowrate at the beginning of the rigid section. This is expressed in non-dimensional terms as:

$$\overline{Q}_R(0) = \frac{1-x_c}{x_c} \frac{\overline{Q}_c(1)}{(1-\varepsilon_c)^3}$$

(6) The resistive parameter for the rigid section is calculated.

$$\beta_R = \frac{(1-x_c)}{(1-\varepsilon_c)^{3/2}} \beta$$

(7) The choice of x_c determines the non-dimensional pressure drop of the system (ε). ε can be determined using Equation (3.3) with $\overline{P}(0) = \varepsilon_c$.

$$\varepsilon = \frac{12\overline{Q}_R(0)(\text{COSH}\,\beta_R - e^{-\beta_R})}{\beta_R} + \varepsilon_c \text{ COSH } \beta_R$$

(8) The non-dimensional flowrate through the rigid section can now be calculated using equation (3.4)

$$\overline{Q}_R(1) = \frac{\varepsilon \beta_R \text{TANH}\beta_R}{12} + \overline{Q}_R(0)e^{-\beta_R}[1 + \text{TANH } \beta_R]$$

(9) Finally, the non-dimension flowrate of the system can be found.

$$\overline{Q} = \frac{(1-\varepsilon_c)^3}{(1-x_c)} \overline{Q}_R(1)$$

Regime II ends when the entire channel is collapsed and fuctioning as a rigid channel. This occurs when x_c becomes zero. ε_R is defined as the ε at which this occurs and is found using equation (3.3)

$$\varepsilon_R = \varepsilon_c \text{ COSH } \left[\frac{\beta}{(1-\varepsilon_c)^{3/2}}\right] \tag{3.5}$$

3.1.3 Results from the rigid septae model. Figure 12 shows the non-dimensional pressure-flow curves for various values of β, with $\varepsilon_c = 0.8$ (if we, somewhat arbitrarily, assume the undeformed height of Schlemm's canal (h_0) to be 30 μm, this corresponds to a post height of 6μm). For small values of β, Regime II is of negligible width ($\varepsilon_c \simeq \varepsilon_R$), and thus there is no apparent slope change between Regime I and Regime III. As β increases, the slope change between Regime I and Regime III increases, and Regime II extends for a larger range of ε.

Figure 13 shows the non-dimensional pressure-flow curves for various values of β, with $\varepsilon_c = 0.9$ (for $h_0 = 30$ μm, this corresponds to a post height of 3μm). For all curves except the smallest β, Regime II extends for a considerable range. As ε_c approaches one, ε_R becomes larger yet and the range of Regime II extends toward infinity.

3.2 Septae Modeled with an Elastic Modulus

The septae preventing complete collapse of Schlemm's canal, although not perfectly rigid, are modeled as such in Section 3.1. Furthermore, it has been assumed that the inner wall does not collapse beyond the effective height of the septae even in between adjacent

septae. In this section we consider the possibility that either the septae are somewhat compliant in their collapsed state, or that the inner wall could collapse around the septae so that the effective channel height might be less than the septae height, h_s.

In Chapter II, the trabecular meshwork is modeled as a set of linear springs holding Schlemm's canal open. Here, we consider the septae to act as linear springs working in conjunction with the trabecular meshwork to keep Schlemm's canal open.

The spring law expressed in Equation (2.3) is valid for $h(x) > h_s$. For $h(x) \leq h_s$, the spring law must include the effect of the septae.

$$IOP - P(x) = E_{TM}\frac{[h_o - h(x)]}{h_o} + E_s\frac{[h_s - h(x)]}{h_s} \qquad h(x) \leq h_s$$

where E_{TM} is the modulus of the trabecular meshwork

E_s is the apparent modulus of the septae

By defining an effective spring modulus (E_{eff}) and an effective undeformed spring height (h_{eff}), the above equation can be rearranged into the form of Equation (2.3).

$$\frac{h(x)-heff}{h_{eff}} = \frac{P(x)-IOP}{E_{eff}} \qquad h(x) \leq h_s \qquad (3.6)$$

where $E_{eff} = E_{TM} + E_s$

$$h_{eff} = h_s \left[\frac{E_s + E_{TM}}{E_s + (h_s/h_o)E_{TM}}\right]$$

The pressure-flow curves for this system are similar to those of the rigid septae model. Three regimes can once again be identified. In Regime I the curves are identical to those of the rigid septae model. Regime II is also very similar since the septae do not change dimension appreciably in this regime. Since we have not solved for the flow in a compliant, porous channel with an input flow at x = 0, the solution for the Regime II characteristics of the rigid septae model will be used to approximate those of the compliant septae model.

The channel is in Regime III when the entire channel has an increased modulus and a decreased undeformed height due to interaction with the septae. The pressure-flow characteristics of this regime are found using the computer program discussed in Chapter II. The procedure used to calculate these parameters follows.

(1) The resistive parameter for this regime is calculated

$$\beta' = \beta\left(\frac{h_o}{h_{eff}}\right)^{3/2}$$

(2) The computer program is used to calculate the smallest ε for which the height of the channel is everywhere less than that of the septae. This is ε_R.

(3) The non-dimensional pressure drop for this regime is defined

$$\varepsilon' \equiv \frac{IOP - P_{cc}}{E_{eff}}$$

(4) ε' is allowed to vary between the minimum calculated in step (2) and 0.9.

(5) The computer program is used to calculate the non-dimensional flowrate

$$\overline{Q}' = \overline{Q}'(\beta', \varepsilon')$$

(6) These non-dimensional variables are not defined in the same way as those in Regimes I & II. They are now converted.

$$\varepsilon = \left(\frac{E_{eff}}{E_{TM}}\right)\varepsilon'$$

$$\overline{Q} = \left(\frac{h_{eff}}{h_o}\right)^3 \left(\frac{E_{eff}}{E_{TM}}\right) \overline{Q}'$$

Figure 14 shows the non-dimensional pressure-flow curves for two values of β, with $\varepsilon_c = 0.8$, and the septae modulus four and eight times that of the trabecular meshwork. The rigid solution is shown for comparison. The curves indicate that unless the septae are very compliant, the changes from the rigid septae model will be imperceptible at low pressures, and have only a moderate effect (less than 20%) at the upper end of the range of normally observed intraocular pressures.

CHAPTER IV

EXPERIMENTAL INVESTIGATION INTO THE PRESSURE-FLOW CHARACTERISTICS OF THE HUMAN EYE

The models discussed in the previous chapters characterize the flow of aqueous humor through Schlemm's canal in the region extending from the midpoint between two collector channels to the collector channel itself. The human eye, however, has approximately thirty collector channels; and the flow path associated with each of them has different geometry and structure, and hence different pressure-flow characteristics. To the extent that the geometrical and structural properties of the trabecular meshwork, the septae and Schlemm's canal are reasonably uniform, one would expect the pressure-flow curve of the human eye to be qualitatively similar to that predicted for the flow path associated with a typical collector channel.

In order to evaluate our theories, we perfused enucleated human eyes and determined their pressure-flow characteristics. Enucleated eyes were used since it is unlikely that active transport plays a role in aqueous outflow (Johnstone and Grant, 1973). No significant changes in the pressure-flow characteristics are expected until tissue degeneration begins.

4.1 Perfusion of the Eye

The perfusion experiments involve the simultaneous determination of intraocular pressure and flowrate through the aqueous outflow network. Although intraocular pressure can be directly measured, the outflow rate cannot; instead we measure the rate of inflow introduced to the posterior chamber. If the volume of the eye remains constant, then the inflow to the posterior chamber must equal the outflow through the aqueous outflow network. However, since the contained volume of the eyes changes with intraocular pressure, increasing the inflow to the eye causes the eye to expand until it reaches a new equilibrium size. Only when it does will inflow equal outflow.

4.1.1 The eye as a fluid capacitor. The eye is a compliant pressure vessel with complex elastic and viscoelastic properties. For a simple approximation, we tenatively model the relation between the intraocular pressure (IOP) and the eye volume (V) as follows:

$$IOP = \frac{(V-V_o)}{C} + b\frac{dV}{dt} \qquad (4.1)$$

where C is the compliance of the eye

b is the viscoelastic coefficient

V_o is the unstressed volume of the eye

The compliance and the viscoelastic coefficient are complex functions of pressure; however, we here consider them constants since this is sufficient for a qualitative description.

The volume change of the eye is a result of the difference between the inflow to the eye (Q_{in}) and the outflow from the eye (Q_{out}).

$$Q_{in} - Q_{out} = dV/dt \qquad (4.2)$$

For this simple approximation, we assume the outflow network to have a constant flow resistance (R_{out}).

$$Q_{out} = \frac{IOP - P_v}{R_{out}} \qquad (4.3)$$

where P_v is the episcleral venous pressure to which the aqueous outflow network empties

We combine Equations (4.1) - (4.3) into a single equation describing the volume change of the eye with an arbitrary inflow.

$$Q_{in} + \frac{P_v}{R_{out}} - \frac{(V-V_o)}{CR_{out}} = \left(1 + \frac{b}{R_{out}}\right)\frac{dV}{dt} \qquad (4.4)$$

Two methods of perfusion are of particular interest because they are easy to realize experimentally: (i) constant rate of inflow, and (ii) constant supply pressure. Each case has associated with it a time constant (τ) indicative of how long it will take to reach 63.2% ($1 - e^{-1}$) of the steady-state value. For the case of constant inflow (Q_{in} = const), the time constant (τ_Q) is

found from Equation (4.4) to be:

$$\text{(i)} \quad \tau_Q = R_{out}C + bC$$

For the case of constant supply pressure, Q_{in} depends on the flow resistance (R_{in}) to the inflow.

$$Q_{in} = (P - IOP)/R_{in}$$

where P is the constant supply pressure

Substituting this relation for Q_{in} into Equation (4.4) and using Equation (4.1), we solve for the time constant (τ_p).

$$\text{(ii)} \quad \tau_p = \frac{R_{out}\, R_{in}}{R_{out} + R_{in}} C + bC$$

The inflow resistance (R_{in}) depends on the equipment used, but is always much less than the outflow resistance (R_{out}); hence, this relation can be approximated.

$$\text{(ii)} \quad \tau_p = R_{in}C + bC$$

The various parameters used in this analysis are not constant, and therefore these estimates of time constants serve only to give the order of magnitude of the length of time required for each pressure-flow data point to reach steady-state. For this estimate, we use the following values:

R_{in} = 0.05 mmHg · min/μL

R_{out} = 4.0 mmHg · min/μL

C = 1.4 μL/mm Hg

b = 6.8 mm Hg · min/μL

The values for R_{in} and R_{out} are typical of the experiments we performed. The values of C and b are typical of those discussed by Collins (1980).

These values yield a time constant for the constant inflow case of 15.1 minutes, and, for the constant supply pressure, of 9.6 minutes. 99% of the steady-state value should be reached after waiting five time constants, and thus constant flow experiments should take approximately seventy-five minutes for each data point, while constant pressure experiments should take approximately fourty-five minutes. In the constant flow experiments discussed later, the time to steady-state was consistent with these predictions: around sixty minutes.

We tried to reduce the time required for each data point by measuring eye circumference using a mercury-in-silastic strain gage from which we could determine the volumetric expansion of the eye. Then, knowing dV/dt, we could use Equation (4.2) to compute Q_{out}. Unfortunately, the magnitude of the strain was so small that it was not possible to discern true changes in circumference from variations caused by changes in mercury temperature. Since changes in mercury temperature as small as 0.1^{o} C per

minute would cause significant errors, we decided that this approach was not practical.

4.1.2 Review of perfusion experiments by other investigators. The use of perfusion experiments to determine the effect of intraocular pressure on the resistance to outflow dates back nearly 100 years (Smith, 1888). As a result of numerous studies, much evidence has accumulated indicating that the resistance to outflow increases with intraocular pressure (see Moses (1977) for a review).

In one of the most comprehensive studies Brubaker (1975) perfused enucleated human eyes imbedded in hydrous calcium sulfate stone to prevent changes in eye volume and found that flow resistance increased linearly with intraocular pressure. The experiments were carefully done, but several objections might be raised. First, it is unclear what affect the calcium sulfate stone would have on the eye. Second, Brubaker presented only averaged data from several different eyes. There is substantial variability between eyes and averaging the data from different eyes masks the true details of individual pressure-flow curves.

Using the constant pressure technique, Ellingsen and Grant (1971) conducted perfusion studies on enucleated human eyes. They concluded that outflow resistance increases as intraocular pressure increases, and that anterior chamber deepening reduces this effect. In their procedure they waited 4 or 5 minutes for the eye to reach steady-state while

averaging the inflow over the entire period. In view of the estimates of time constant made above, this may not have been sufficient for the eye to come to steady-state. Their data on the effect of prolonged perfusion time on resistance tend to support this possibility.

Levene and Hyman (1969) measured the outflow resistance of *in vivo* human eyes using tonographic techniques. They also investigated the effects of pressure elevation on outflow resistance. Although their techniques involved considerable uncertainty, several interesting conclusions were reached. They found resistance to increase as the intraocular pressure increased; however, they found that resistance reached a maximum and remained nearly constant as intraocular pressure was further increased. This is consistent with the predictions of the model discussed in Chapter III. They also found that the resistance increased less in eyes with high initial resistance.

Although many studies have been conducted, the literature contains little information on the pressure-flow characteristics of human eyes at high pressures (50 - 100 mm Hg). Also, in most studies, the results from many eyes were averaged. For these reasons, the literature is not well suited to a critical assessment of our theories and we decided to conduct our own experiments. The objectives of present study then, was to investigate the pressure-flow curves of individual eyes over a wide range of intraocular pressures.

4.2 The Present Perfusion Experiments

We were fortunate during our experiments to be permitted to use a perfusion device newly designed by Dr. P. John Anderson of the Massachusetts Eye and Ear Infirmary. The studies were preliminary in the sense that we were learning the experimental procedure, and there were insufficient enucleated human eyes to do a full-scale study.

4.2.1 Description of the perfusion apparatus. Figure 15 shows two views of the perfusion apparatus: two syringe pumps and their associated electronics are on the cart along with pressure and flow measurement electronics; the experimental setup for perfusing the eye is on the table. The left syringe pump is connected via plastic tubing to the experimental setup on the table.

A schematic of the system is shown in Figure 16. The syringe pump drives fluid into the eye at a constant rate while the pressure transducer monitors pressure just upstream from the eye. Figure 17a shows the experimental setup without the connection to the syringe pump. The refill reservoir is seen at the top of the picture, the pressure transducer in the middle and the syringe for backfilling the system at the bottom-left. At the bottom-right of the picture is a calf eye in a beaker.

The eye to be perfused is placed in a beaker containing several gauze pads; the beaker is filled with saline. The surface of the eye is then wrapped with saline-wetted gauze.

Figure 17b shows a close up of the calf eye. The needle carrying the perfusion fluid can be seen to pass through the cornea and then disappear behind the iris. The tip of the needle is placed behind the iris, in the posterior chamber, to prevent anterior chamber deepening which is known to affect outflow resistance.

4.2.2 The experimental routine. In preparation for experimentation, the pressure sensor and syringe pump were calibrated. The resistance between the pressure sensor and the eye was measured and found to be negligible (0.05 mmHg · min/μL).

The perfusion fluid was Dulbecco's phosphate buffered saline to which glucose was added (5.5 mM). This solution was selected because it is known to cause a minimal wash-out effect (the decrease in outflow resistance with time). The solution is passed through a micropore filter, and then used to fill the system while attempting to eliminate all bubbles.

The enucleated eyes are usually received about twenty-four hours after death. The eye to be perfused is placed in a beaker (as described above) which is maintained at a constant temperature of 72^{o} F. This temperature is significantly less than the physiologic temperature and thus the viscosity of the perfusion fluid is increased correspondingly (by about 40%). This causes an increase in the measured resistance.

A 23 gauge needle is passed through the cornea, maintaining a constant flow of perfusate to prevent occlusion of

the needle. The cornea seals around the needle. The tip of the needle is placed behind the iris. The eye is then allowed to remain for one hour with no flow to establish zero pressure.

The experiments were run in constant flow mode, although in some instances we attempted to adjust the flowrate to achieve steady-state more quickly. Steady-state was determined to occur when the pressure reading remained constant for five minutes. The observed time to steady-state varied between one half hour and one hour.

The pressure uncertainty is calculated as follows:

PRESSURE UNCERTAINTY	=	PRESSURE SENSOR ERROR	+	ZERO DRIFT ERROR	+	NOISE	+	END POINT UNCERTAINTY

The pressure sensor error is approximately 0.25 mm Hg and the zero drift is estimated at 0.25 mm Hg. The noise and the end point uncertainty (uncertainty as to whether the experiment has reached steady-state) were estimated for each data point from the strip chart recording of pressure. The measurement of flow are accurate to within 0.5%.

4.2.3 The experimental results. The results from the perfusion experiments are shown in Table II and Figures 18-20. The figures show open symbols for one eye of the pair and closed symbols for the other. The numbers below the closed symbols (and above the open symbols) indicate the order in which the data were acquired. The dashed line on the figures -- having the same general form as the curves predic-

ted in Chapter III -- is included only to demonstrate that the data are consistent with, but by no means confirm the theoretical predictions.

Although four pairs of eyes were tested, we are confident only of the results obtained on the fourth pair. We believe, however, that the results obtained on the first two pairs of eyes (Tables IIa and IIb and Figures 18 and 19) are qualitatively correct in spite of some error due to a small leak past the syringe. The leaky syringes were replaced by leakproof syringes prior to testing the fourth pairs of eyes (Table IIc and Figure 20).

4.3 Analysis of the Experimental Data

As stated above, the experiments were preliminary and more data are necessary before we can reach any definite conclusions. Still, it is useful to calculate representative values of the various parameters pertaining to the theory.

4.3.1 Parameters describing the shape of the pressure-flow curve. To calculate representative values of the non-dimensional parameters which describe the pressure-flow curve, the data from the fourth pair of eyes (Table IIc and Figure 20) are used, as these are the data most likely to be reliable. From these results, we will estimate four parameters of the model: the pressure at which Schlemm's canal has first collapsed, the pressure at which the entire canal is collapsed and the slopes of the pressure-flow curve both above and below

these pressures. This information will then be used to determine numerical values for ε_c, ε_R, β^2 and E.

The shape of the pressure-flow curve in Figure 20 is suggestive of the models discussed in Chapter III (rigid or compliant septae). Equation (3.5) relates the non-dimensional pressure at which the inner wall of Schlemm's canal has first collapsed to the effective height of the septae (ε_c), to the non-dimensional pressure at which Schlemm's canal is first entirely collapsed (ε_R).

$$\varepsilon_R/\varepsilon_c = \text{COSH}\left[\frac{\beta}{(1-\varepsilon_c)}3/2\right]$$

ε_c is located on Figure 20 at data point 7, while ε_R is located just past data point 9. We find that $\varepsilon_R/\varepsilon_c = 1.8$. Figure 11 shows the relationship between the slope in Regime I and the slope in Regime III.

$$\frac{d\bar{Q}/d\varepsilon\big|_{\varepsilon=\varepsilon_R}}{d\bar{Q}/d\varepsilon\big|_{\varepsilon=\varepsilon_c}} = \frac{(1-\varepsilon_c)^{3/2}\ \text{TANH}\left[\beta/(1-\varepsilon_c)^{3/2}\right]}{\text{TANH}\ \beta}$$

From Figure 20 this ratio of slopes is found to be 0.70. These two equations are solved simultaneously for β and ε_c yielding:

$$\beta = 0.11 \qquad \varepsilon_c = 0.79,$$

Therefore ε_R equals 1.36.

The value of ε_c can be used to determine the spring constant (E) of the trabecular meshwork.

$$\varepsilon_c = \Delta p_c / E$$

where Δp_c is the pressure drop corresponding to ε_c.

The pressure drop corresponding to ε_c is 15.4 mm Hg. Therefore, E can be estimated.

$$E = 19.4 \text{ mm Hg.}$$

From the definition of β^2 in Chapter II, we find:

$$\beta^2 = \frac{\text{RESISTANCE TO FLOW IN SCHLEMM'S CANAL IN THE UNDEFORMED STATE}}{\text{RESISTANCE TO FLOW THROUGH THE INNER WALL OF SCHLEMM'S CANAL}} = 0.013$$

This is consistent with the conclusions reached by Moses (1981) that most of the resistance to outflow occurs in the inner wall of Schlemm's canal.

These values are only meant to be estimates as they could change significantly depending on the error range. This represents one, but certainly not the only interpretation of the data.

4.3.2 The inner wall resistance. If these preliminary conclusions can be verified by additional experiments, it appears likely that most of the outflow resistance occurs in the inner wall of Schlemm's canal. It is therefore interesting to speculate on the nature of this resistance. We might assume that the inner wall resistance occurs in pores which are 10μm in length and 1.5 μm in diameter. The pore diameter

is based on perfusion studies which used tracers to determine the smallest flow dimensions (Huggert, 1955); the length of the pores is admittedly arbitrary but is certainly the right order of magnitude. The pressure drop through these pores can be calculated using the following formula (Dagan, Weinbaum and Pfeffer, 1979):

$$\Delta P = (3 + 8L/\pi r) \frac{\mu Q}{r^3}$$

where r is the radius of the pore

L is the length of the pore

The first term on the right hand side of the equation represents the pressure loss of fluid traveling to the pore; the second term, the pressure drop caused by the Poiseuille flow through the pore. This formula neglects the entrance length in the pore for developing the Poiseuille profile, however this has recently been shown to be insignificant (Eriksson and Svedbergh, 1980).

The flowrate (Q) is set equal to 2.0/N μL/min, where N is the number of pores. For a pressure drop of 6 mm Hg, we find that N=1400 (130 pores/mm^2). This number is significantly smaller than the 23,000 pores found by Bill and Svedbergh (1972), but it is consistent with the number of endothelial tubules (2000) found by Johnstone (personal communication).

4.3.3 Implications for glaucoma. The spring constant for the trabecular meshwork estimated above -- approximately 20 mm Hg -- is roughly consistent with the studies done by Johnstone and Grant (1973) on the pressure-dependent changes of the trabecular meshwork. Certainly, when the intraocular pressure is 50 mm Hg., the trabecular meshwork is completely expanded and Schlemm's canal is completely collapsed. Yet the outflow resistance at 50 mm Hg, measured by several investigators, is not high enough to cause glaucoma. This suggests that glaucoma is *not* caused by a weakening of the trabecular meshwork and a resultant collapse of Schlemm's canal alone.

CHAPTER V

CONCLUSIONS AND SPECULATIONS

The experimental data contained within this study are not sufficient to draw any definite conclusions. However, when we combine our theoretical results with the experimental evidence from other investigators, a number of interesting conclusions arise.

(1) Most of the pressure drop in the aqueous outflow network occurs in the inner wall of Schlemm's canal.

Most experimental investigations (including the present ones) have only found small non-linearities in the aqueous outflow curves for human eyes. If Schlemm's canal contributed significantly to the total outflow resistance, then changes in its dimensions -- caused by changes in the intraocular pressure -- would lead to large changes in resistance. Since only small changes in resistance occur as the intraocular pressure is changed, Schlemm's canal resistance must be a small part of the total resistance.

In Section 1.3.2 and 1.3.4 we discuss why the trabecular meshwork and the aqueous veins are unlikely to cause significant flow resistance. Therefore, the inner wall of Schlemm's canal appears to be the major source of resistance. The Na_2 EDTA studies (Bill and Svedbergh, 1980) discussed in Section 1.3.2 suggest that the juxtacanalicular meshwork is the primary site of resistance within the inner wall.

(2) Significant collapse of Schlemm's canal occurs only when the intraocular pressure is substantially elevated.

The estimated experimental value for the spring constant (E) of the trabecular meshwork of 20 mm Hg is consistent with other observations of meshwork distension (Johnstone and Grant, 1973). Therefore, a normal pressure drop through the aqueous outflow network of 6 mm Hg is equivalent to $\varepsilon = 0.3$. Figure 6 shows that for $\varepsilon = 0.3$ and $\beta = 0.1$, the model predicts that Schlemm's canal is nearly wide open. Recent work by Moses (1981) supports this conclusion.

(3) The assumption that the inner wall resistance occurs in pores which are 10μm in length and 1.5 μm in diameter leads to the conclusion that there are approximately 1400 of these pores in the eye.

In Section 4.3.2, we show that 1400 pores are necessary to pass the flowrate of 2.0 μL/min at a pressure drop of 6 mm Hg.

(4) Glaucoma is *not* caused by a weakening of the trabecular meshwork and a resultant collapse of Schlemm's canal alone. Glaucoma is likely caused by a decreased porosity of Schlemm's canal inner wall.

If we accept that the spring constant for the trabecular meshwork is approximately 20 mm Hg, then Schlemm's canal is certainly collapsed when the intraocular pressure is 50 mm Hg. Yet the resistance at 50 mm Hg, measured by several investigators, is not high enough to cause glaucoma.

Two possible explanations could be proposed: Although weakening of the trabecular meshwork alone would not cause glaucoma, a concurrent weakening of the septae, which normally prevent the collapse of Schlemm's canal, could. However, a seemingly more likely possibility would be that glaucoma is caused by a decrease of inner wall porosity.

APPENDIX A

```
C                INTEGRATION FOR H(X)
C
      SUBROUTINE SCHLEM(E,B,Q)
      DIMENSION H(1001)
      PARAMETER NMAX=1001
C
C              START PROGRAM
C
      H1=1.-E
      TOP=1.
      BOTTOM=H1
      N=1
100   HO=(TOP+BOTTOM)/2.
      CALL INTEG(H1,B,HO,*300,H)
      L=1
      IF(ABS(HO-H(NMAX)).LE.3.E-07) GO TO 200
      GO TO 110
300   L=0
110   N=N+1
      IF(N.GT.25) GO TO 400
      IF(L.EQ.0) GO TO 120
      TOP=HO
      GO TO 100
120   BOTTOM=HO
      GO TO 100
200   CALL DERIVH(H1,H(NMAX),B,*400,VALUE)
      Q=(H1**3)*VALUE/12.
      WRITE(6,1001) Q,H(NMAX),H(2),N
      SUM=0.
      DO 500 I=1,1001
      WRITE(10,1005) I,H(I)
      SUM=SUM+H(I)
500   CONTINUE
      SUM=SUM/1001.
      WRITE(10,1006) SUM
1005  FORMAT(5X,I5,F10.5)
1006  FORMAT(20X,F10.5)
      RETURN
C                ERRORS
400   WRITE(6,1002) N,HO,H(NMAX)
      STOP
1000  FORMAT(F10.5)
1001  FORMAT(10X,3F12.7,I5)
1002  FORMAT(10X,'ERROR',5X,I5,2F10.5)
1003  FORMAT(2X,' H1 = ',$)
1004  FORMAT(2X,' B  = ',$)
      END
C
C
```

```
      SUBROUTINE INTEG(H1,B,HO,*,H)
      DIMENSION H(1001),VALUE(1001),PSUM(1001)
      PARAMETER NMAX=1001
C     INPUT   H1: H(1)
C             HO: GUESSED VALUE FOR H(O)
C             B:  BETA
C             F:  DERIVATIVE OF H WITH RESPECT TO X
C             *:  RETURN FOR H(X) .GT. H(O)
C     OUTPUT  H:  H(N)  N=1,NMAX
C
      DELTAX=1./FLOAT(NMAX-1)
      H(1)=H1
      CALL DERIVH(H1,HO,B,*200,VALUE(1))
      PSUM(1)=H1+VALUE(1)*DELTAX/3.
      DO 100 N=2,NMAX-1
      CONST=2.
      IF((N/2)*2.EQ.N) CONST=4.
      IF(N.LE.3) GO TO 250
      HGUESS=(3.*H(N-1)-4.*H(N-2)+H(N-3))/2.+H(N-1)
50    CALL DERIVH(HGUESS,HO,B,*200,VALUE(N))
      PSUM(N)=PSUM(N-1)+CONST*VALUE(N)*DELTAX/3.
      IF((N/2)*2.EQ.N) GO TO 300
      H(N)=PSUM(N-1)+VALUE(N)*DELTAX/3.
      GO TO 100
300   IF(N.EQ.2) GO TO 350
      H(N)=H(N-3)+(VALUE(N-3)+3.*(VALUE(N-2)+VALUE(N-1))
     C      +VALUE(N))*3.*DELTAX/8.
      GO TO 100
350   D2=(B**2)*(H(1)-1.)/(H(1)**3)-3.*(VALUE(1)**2)/H(1)
      H(2)=H(1)+VALUE(1)*DELTAX+D2*(DELTAX**2)
100   CONTINUE
      H(NMAX)=H(NMAX-1)
      IF(H(NMAX).GT.HO) GO TO 200
      RETURN
250   CALL DERIVH(H(N-1),HO,B,*200,VALUE(N))
      HGUESS=H(N-1)+VALUE(N)*DELTAX
      GO TO 50
200   RETURN 1
      END
```

```
C
      SUBROUTINE DERIVH(H,HO,B,*,VALUE)
      TERM1=(HO**4)/4.-(HO**5)/5.
      TERM2=(H**4)/4.-(H**5)/5.
      IF(TERM1.LT.TERM2) GO TO 100
      VALUE=B*SQRT(2.*(TERM1-TERM2))/(H**3)
      RETURN
C     ERROR RETURN
100   RETURN 1
      END
```

REFERENCES

Battaglioli, J.L. (1981); "The Role of Vessel Collapse on the Flow of Aqueous Humor," Masters Thesis, Department of Mechanical Engineering, M.I.T., June, 1981.

Bill, A., and Svedbergh, B. (1972); "Scanning Electron Microscopic Studies of the Trabecular Meshwork and the Canal of Schlemm - An Attempt to Localize the Main Resistance to Outflow of Aqueous Humor in Man," Acta Ophthalmologica 50: 295-320.

Bill, A., Lütjen-Drecoll E., and Svedbergh, B. (1980); "Effects of Intracameral Na_2 EDTA and EGTA on Aqueous Outflow Routes in the Monkey Eye," Investigative Ophthalmology 19, 5: 492-504.

Brubaker, R.F. (1975); "The Effect of Intraocular Pressure on Conventional Outflow Resistance in the Enucleated Human Eye," Investigative Opthalmology 14, 4: 286-292.

Collins, R. and van der Wereff, T.J. (1980), Mathematical Models of the Dynamics of the Human Eye, Springer-Verlag, New York.

Conte, S.D. and deBoor, C. (1965); Elementary Numerical Analysis, McGraw-Hill, New York.

Ellingsen, B.A. and Grant, W.M. (1971); "The Relation of Pressure and Aqueous Outflow in Enucleated Human Eyes," Investigative Ophthalmology 10, 6: 430-437.

Eriksson, A. and Svedbergh, B. (1980); "Transcellular Aqueous Humor Outflow: A Theoretical and Experimental Study, Grafes Archiv Ophthalmologie, 212.

Friedland, A.B. (1978); "A Hydrodynamic Model of Aqueous Flow in the Posterior Chamber of the Eye," Bulletin of Mathematical Biology 40: 223-235.

Fung, Y.C., Sobin, S.S. (1977); "Pulmonary Alveolar Blood Flow", Chapter 4 in Bioengineering Aspects of the Lung, Ed. J.B. West, Marcel Dekker Inc.

Hoffmann, F. and Dumitrescu, L. (1971); "Schlemm's Canal under the Scanning Electron Microscope," Ophthalmology Research 2: 37-45.

Huggert, A. (1955); "Pore Size in the Filtration Angle of the Eye," ACTA OPHTHAL Kbh. 33: 271-284.

Huggert, A., Holmberg, A., and Esklund, A. (1955); "Further Studies Concerning Pore Size in the Filtration Angle of the Eye," ACTA OPHTHAL Kbh. 33: 429-435.

Johnstone, M.A. and Grant, W.M. (1973); "Pressure-Dependent Changes in Structures of the Aqueous Outflow System of Human and Monkey Eyes," American Journal of Ophthalmology 75, 3: 365-383.

Johnstone, M.A. (1974); "Pressure Dependent Changes in the Configuration of the Endothelial Tubules of Schlemm's Canal," American Journal of Ophthalmology 78: 630-638.

Kenyon, D.E. (1980); "A Model for Surface Flow in Cartilage," Journal of Biomechanics 13: 129-134.

Levene, R. and Hyman, B. (1969); "The Effect of Intraocular Pressure on the Facility of Outflow," Experimental Eye Research 8: 116-121.

Moses, R.A. (1970); Adler's Physiology of the Eye, 5th Edition; C.V. Mosby Co.; St. Louis.

Moses, R.A. (1977); " The Effect of Intraocular Pressure on Resistance to Outflow," Survey of Ophthalmology 22, 2: 88-100.

Moses, R.A. (1979); "Circumferential Flow in Schlemm's Canal," American Journal of Ophthalmology 88: 585-591.

Moses, R.A., Grodzki, W.J. Jr., Etheridge, E.L. and Wilson, C.D. (1981); "Schlemm's Canal: The Effect of Intraocular Pressure," Investigative Ophthalmology 20,1: 61-68.

Richardson, T.M., Hutchinson, T., and Grant, W.M. (1977); "The Outflow Tract in Pigmentary Glaucoma," Archives of Ophthalmology 95: 1015-1025.

Smith, P. (1888); "On the Escape of Fluid from the Aqueous and Vitreous Chambers under Different Pressures," Ophthalmol Rev 7: 193-208.

Tripathy, R.C. (1971); "Mechanism of the Aqueous Outflow across the Trabecular Wall of Schlemm's Canal," Experimental Eye Research 11: 116-121.

Tripathy, R.C. (1974); "Comparative Aspects of Aqueous Outflow," Chapter 3 in The Eye, Vol. 5: Comparative Physiology, Ed H. Davson, pp. 163-241, Academic Press, London and New York.

TABLE I

	COMPLIANT CHANNEL	RIGID CHANNEL	SYSTEM
REGION OF CHANNEL	$0 \leq x' \leq x_c$	$x_c \leq x' \leq 1$	$0 \leq x' \leq 1$
LENGTH	$x_c s$	$(1 - x_c)\, s$	s
UNDEFORMED HEIGHT	h_o	$(1 - \varepsilon_c)\, h_o$	h_o
NON-DIMENSIONAL FLOWRATE	$\overline{Q}_c \left(\frac{x'}{x_c}\right) = x_c\, \overline{Q}\,(x')$	$\overline{Q}_R \left(\frac{x' - x_c}{1 - x_c}\right) = \frac{\left(1 - x_c\right)}{\left(1 - \varepsilon_c\right)^3} Q\,(x')$	$Q\,(x') = \frac{\mu\, Q\,(x')\, s}{w\, h_o^3\, E}$
	$Q_c \equiv Q_c\,(1)$	$Q_R \equiv Q_R\,(1)$	$Q \equiv Q\,(1)$
RESISTANCE PARAMETER	$\beta_c = x_c \beta$	$\beta_R = \frac{(1 - x_c)}{\left(1 - \varepsilon_c\right)^{3/2}}\ \beta$	$\beta = \sqrt{\frac{12\ us/wh_o^3}{R_w/s}}$

TABLE II

PRESSURE-FLOW DATA FROM ENUCLEATED HUMAN EYES

	FIRST EYE			SECOND EYE		
	FLOW (μL/min)	PRESSURE (mm Hg)	PRESSURE UNCERTAINTY (mm Hg)	FLOW (μL/min)	PRESSURE (mm Hg)	PRESSURE UNCERTAINTY (mm Hg)
(a) 86 years old; 33 hours after death *	2.99	9.76	+1.5/-0.5			
	1.49	4.34	±0.5			
	4.70	20.4	±0.5			
	5.29	25.0	+1.5/-0.5			
	7.32	36.0	±1.0			
	8.01	41.6	±2.0			
	(see figure 18)					
(b) 68 years old; 21 hours after death	0.97	1.95	±0.5	2.10	5.95	±0.5
	1.61	3.04	±0.5	3.35	9.14	±0.5
	1.26	3.15	±0.5	11.2	> 40	
	2.35	7.57	±0.5	14.7	> 61	
	3.16	9.14	±0.5	12.6	> 56	
	4.20	11.08	±0.5	9.47	35.6	+1.5/-0.5
	5.60	17.1	+1.0/-0.5			
	6.66	20.4	±0.5			
	(see closed symbols on figure 19)			(see open symbols on figure 19)		
(c) 48 years old; 19 hours after death	3.46	10.22	+1.0/-0.5	1.69	5.62	±1.0
	1.67	4.54	±0.5	10.23	53.4	+1.0/-1.5
	1.01	2.92	±0.5	9.12	44.1	±1.0
	2.24	8.06	+1.0/-0.5	8.19	36.9	±1.0
	2.68	10.16	+0.5/-1.5	7.52	35.8	±1.0
	0.56	1.95	+0.5/-1.0	1.51	4.33	±0.5
				4.18	15.52	±1.0
				2.67	9.35	±0.5
				5.30	25.7	±0.5
	(see closed symbols on figure 20)			(see open symbols on figure 20)		

*No measurements on second eye.

FIGURE CAPTIONS

Fig. 1. Outline of the aqueous humor circulatory system

Fig. 2. Micrograph of the trabecular meshwork and Schlemm's canal (Tripathy, 1974). SC- Schlemm's canal, TM- Trabecular meshwork, CSW- Corneoscleral wall, CC- Collector channel, S- Septae.

Fig. 3. Schematic showing the effect of intraocular pressure on the trabecular meshwork and Schlemm's canal (Johnstone and Grant, 1973).

Fig. 4. Model of Schlemm's canal as a porous, compliant channel.

Fig. 5. Degree of collapse as a function of distance along the channel, $\beta^2 = 0.0036$.

Fig. 6. Degree of collapse as a function of distance along the channel, $\beta^2 = 0.01$.

Fig. 7. Degree of collapse as a function of distance along the channel, $\beta^2 = 0.25$.

Fig. 8. Flowrate vs. pressure drop for $0.02 < \beta < 0.10$.

Fig. 9. Flowrate vs. pressure drop for $0.2 < \beta < 0.5$.

Fig. 10. Model of Schlemm's canal as a porous, compliant channel with complete collapse prevented by septae.

Fig. 11. Schematic of typical pressure-flow curve for rigid septae model.

Fig. 12. Flowrate vs. pressure drop for the rigid septae model. $\varepsilon_c = 0.8$, $0.02 < \beta < 0.10$.

Fig. 13. Flowrate vs. pressure drop for the rigid septae model. $\varepsilon_c = 0.9$, $0.02 < \beta < 0.10$.

Fig. 14. Flowrate vs. pressure drop for the compliant septae model. $\beta = 0.06$ and 0.10.

Fig. 15. Photograph of perfusion apparatus.

Fig. 16. Schematic of perfusion system.

Fig. 17a. Photograph of refill reservoir, pressure transducer and back-filling syringe.

Fig. 17b. Photograph of a calf eye being perfused.

Fig. 18. Pressure-flow data from first pair of eyes.

Fig. 19. Pressure-flow data from second pair.

Fig. 20. Pressure-flow data from third paid of eyes.

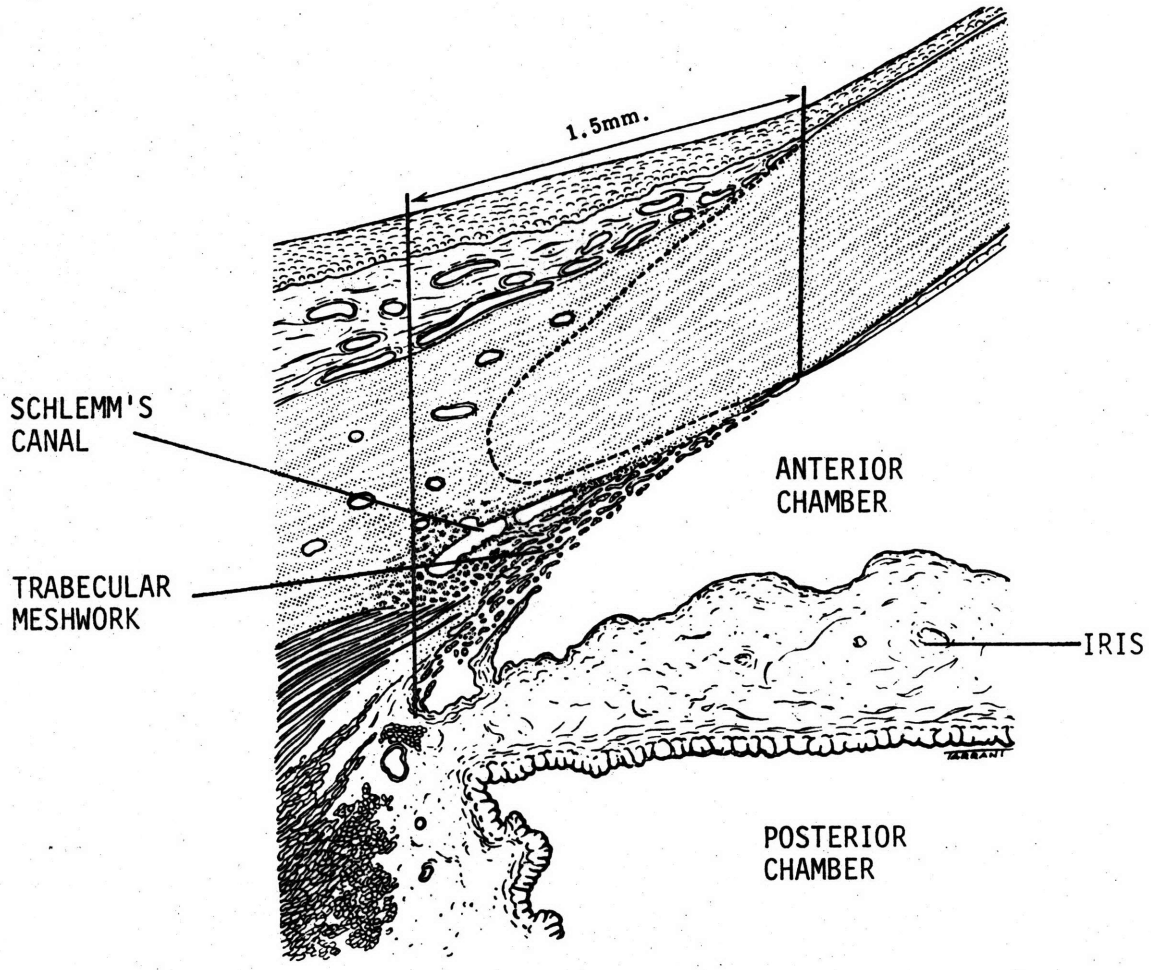
1.5mm.
SCHLEMM'S
CANAL
TRABECULAR
MESHWORK
ANTERIOR
CHAMBER
IRIS
POSTERIOR
CHAMBER

Figure 1

Figure 2

LOW INTRAOCULAR PRESSURE

HIGH INTRAOCULAR PRESSURE

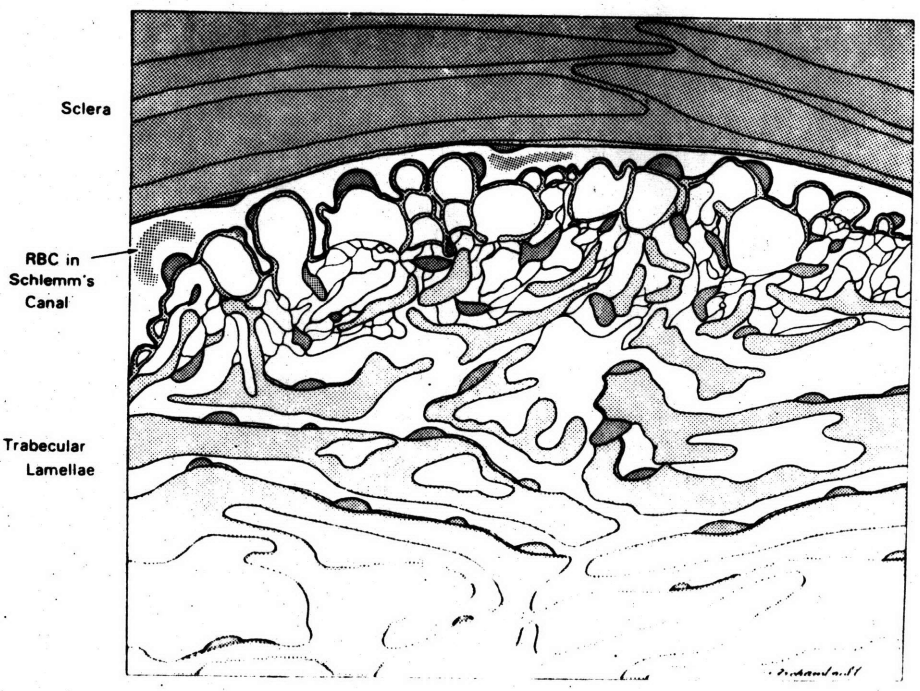

Figure 3

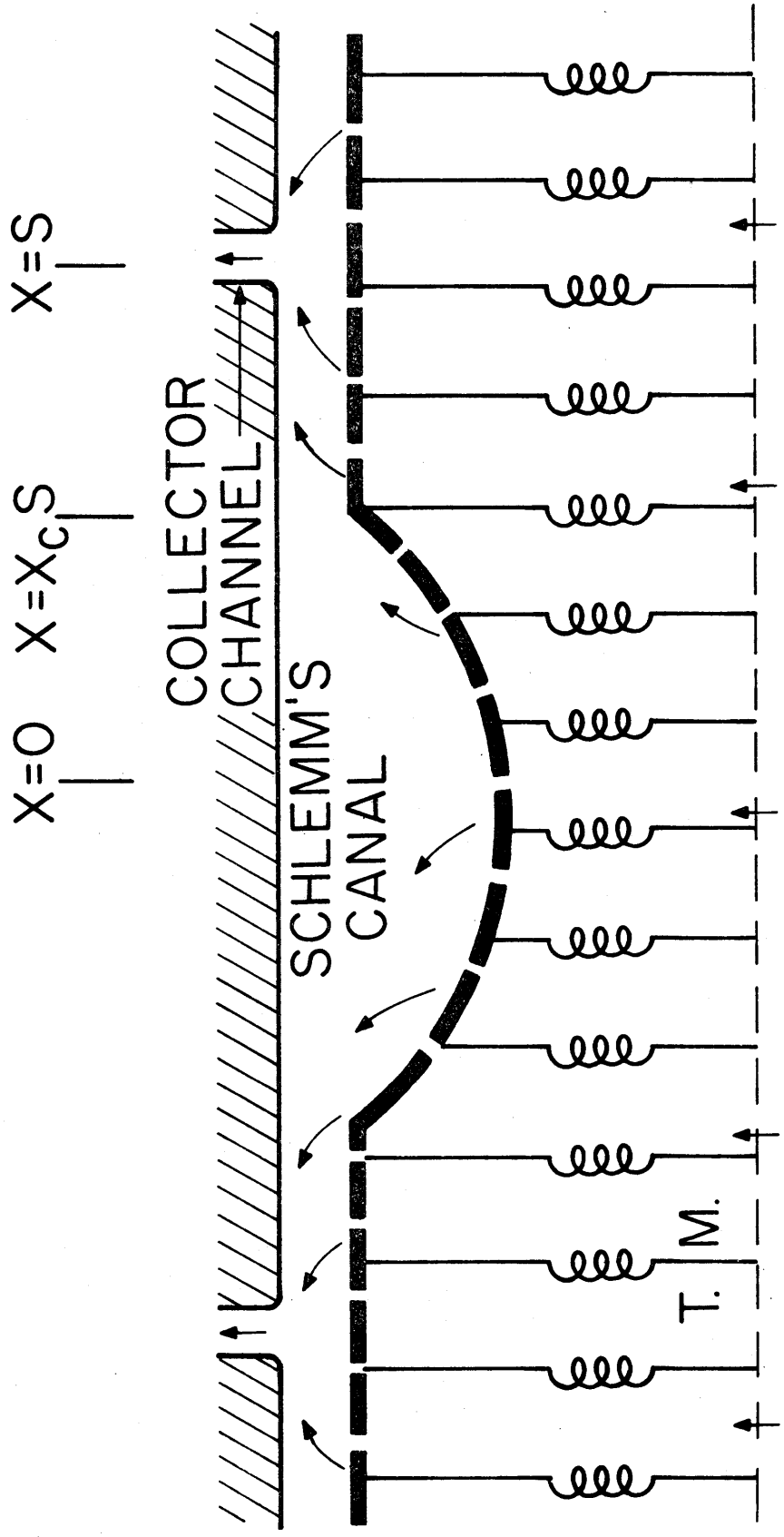
X=O
X=XcS
X=S
COLLECTOR CHANNEL
SCHLEMM'S CANAL
T. M.
INTRAOCULAR PRESSURE (IOP)

Figure 4

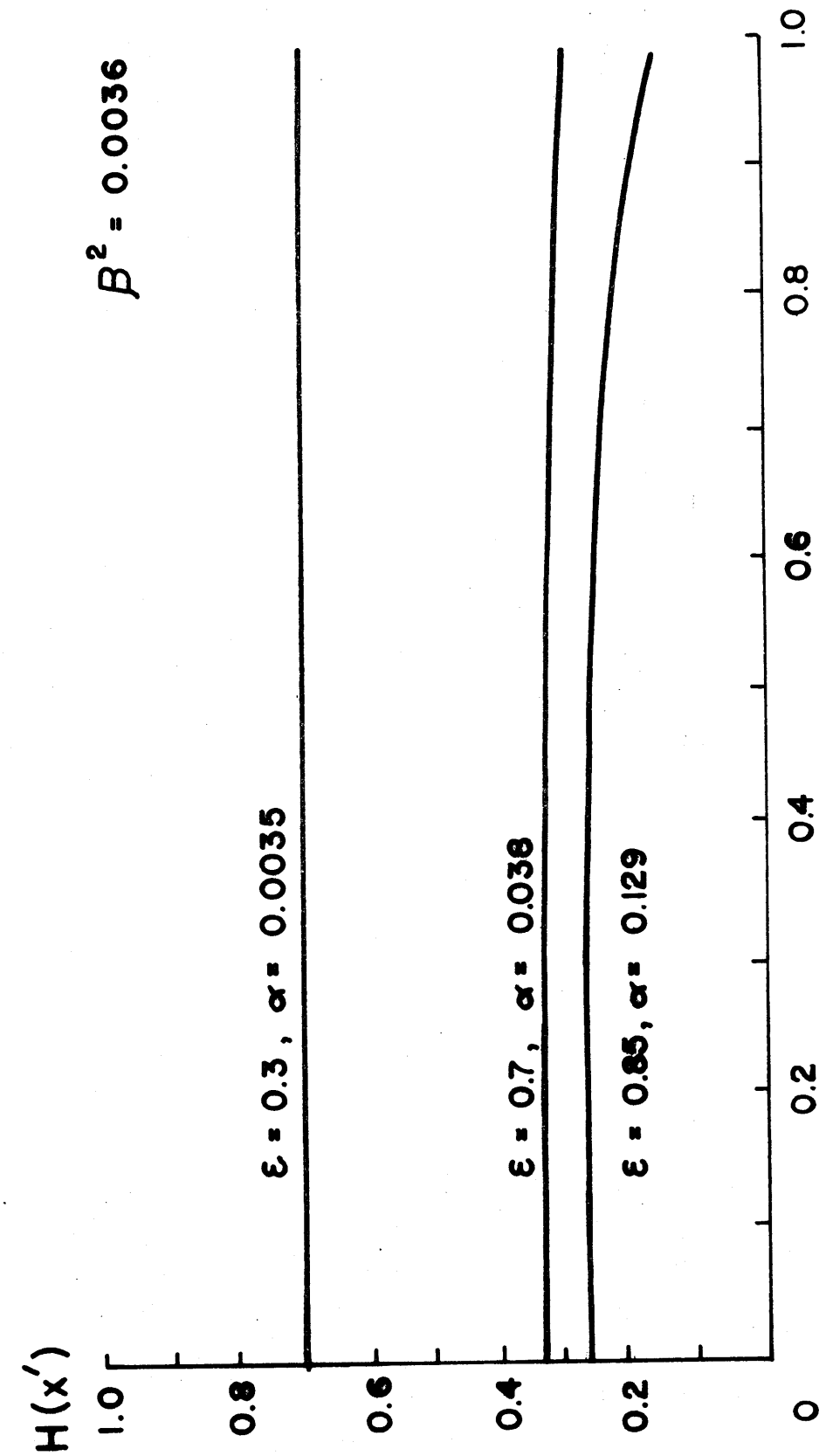
$B^2 = 0.0036$
$\varepsilon = 0.3, \alpha = 0.0035$
$\varepsilon = 0.7, \alpha = 0.038$
$\varepsilon = 0.85, \alpha = 0.129$
H(x')
1.0
0.8
0.6
0.4
0.2
0
0.2
0.4
0.6
0.8
1.0
x' = x/s

Figure 5

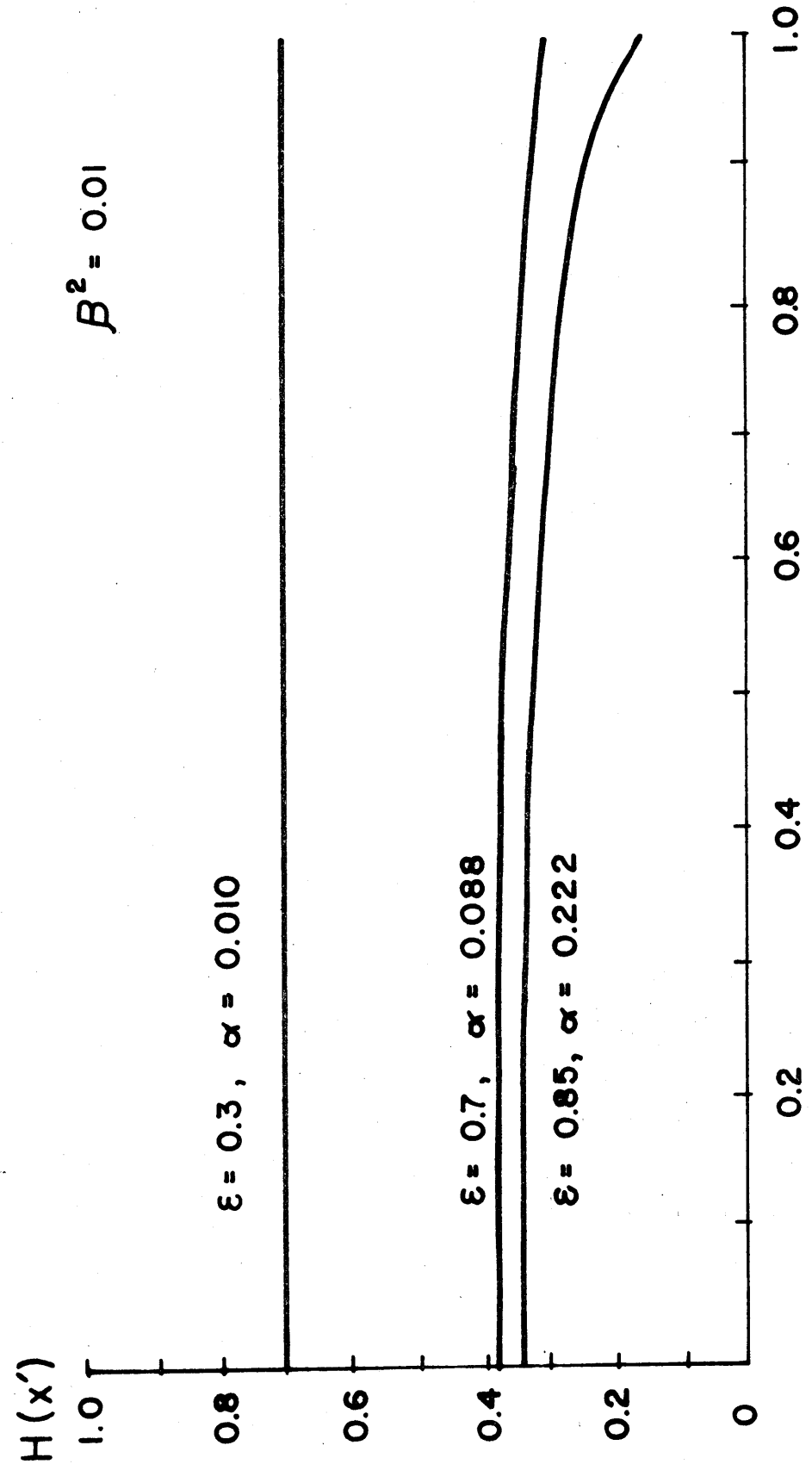
H(x')
1.0
0.8
0.6
0.4
0.2
0
0.2
0.4
0.6
0.8
1.0
x' = x/s
B^2 = 0.01
ε = 0.3, α = 0.010
ε = 0.7, α = 0.088
ε = 0.85, α = 0.222

Figure 6

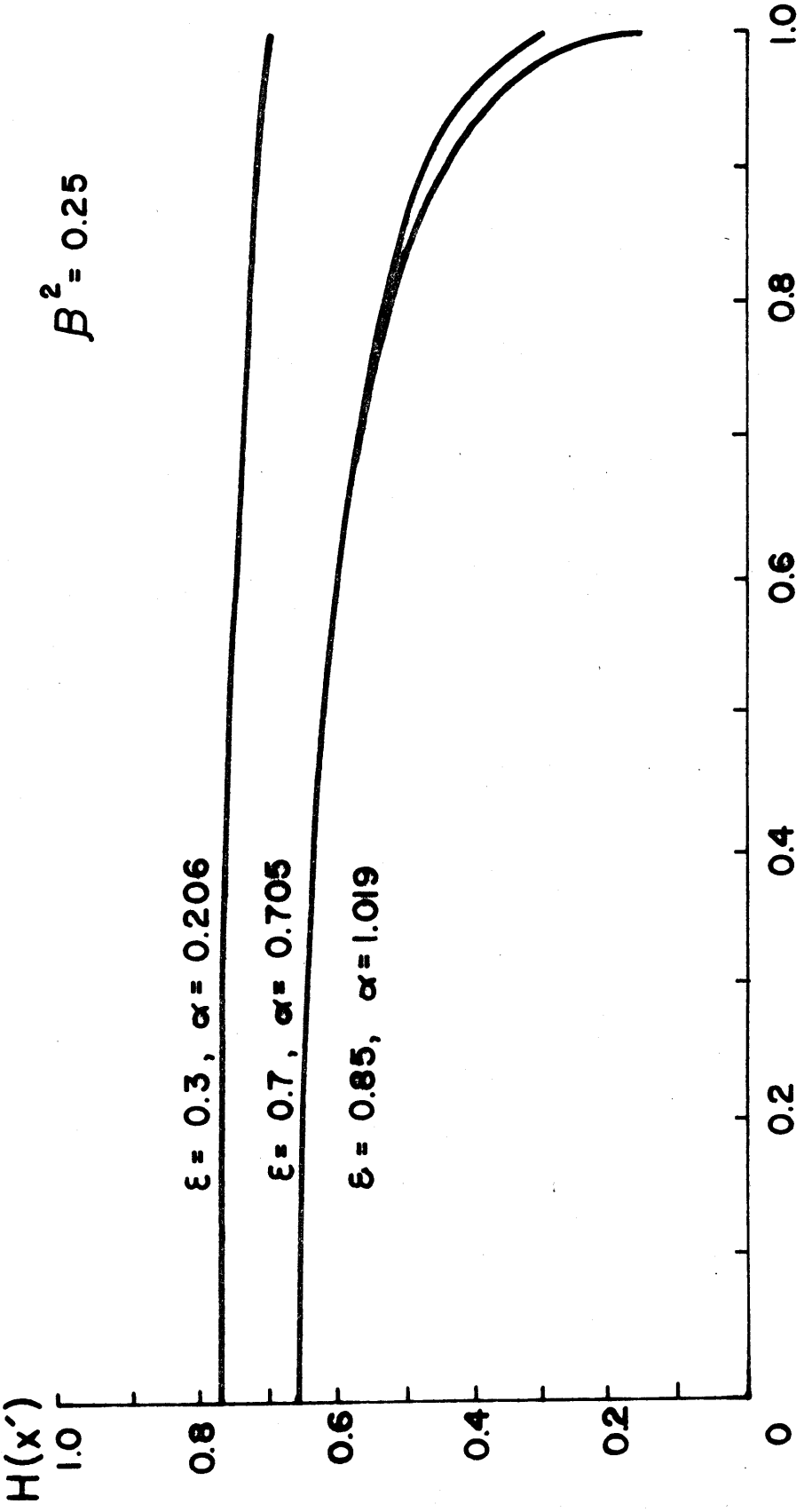
$B^2 = 0.25$
$\varepsilon = 0.3$, $\alpha = 0.206$
$\varepsilon = 0.7$, $\alpha = 0.705$
$\varepsilon = 0.85$, $\alpha = 1.019$
H(x')
1.0
0.8
0.6
0.4
0.2
0
0.2
0.4
0.6
0.8
1.0
$x' = x/s$

Figure 7

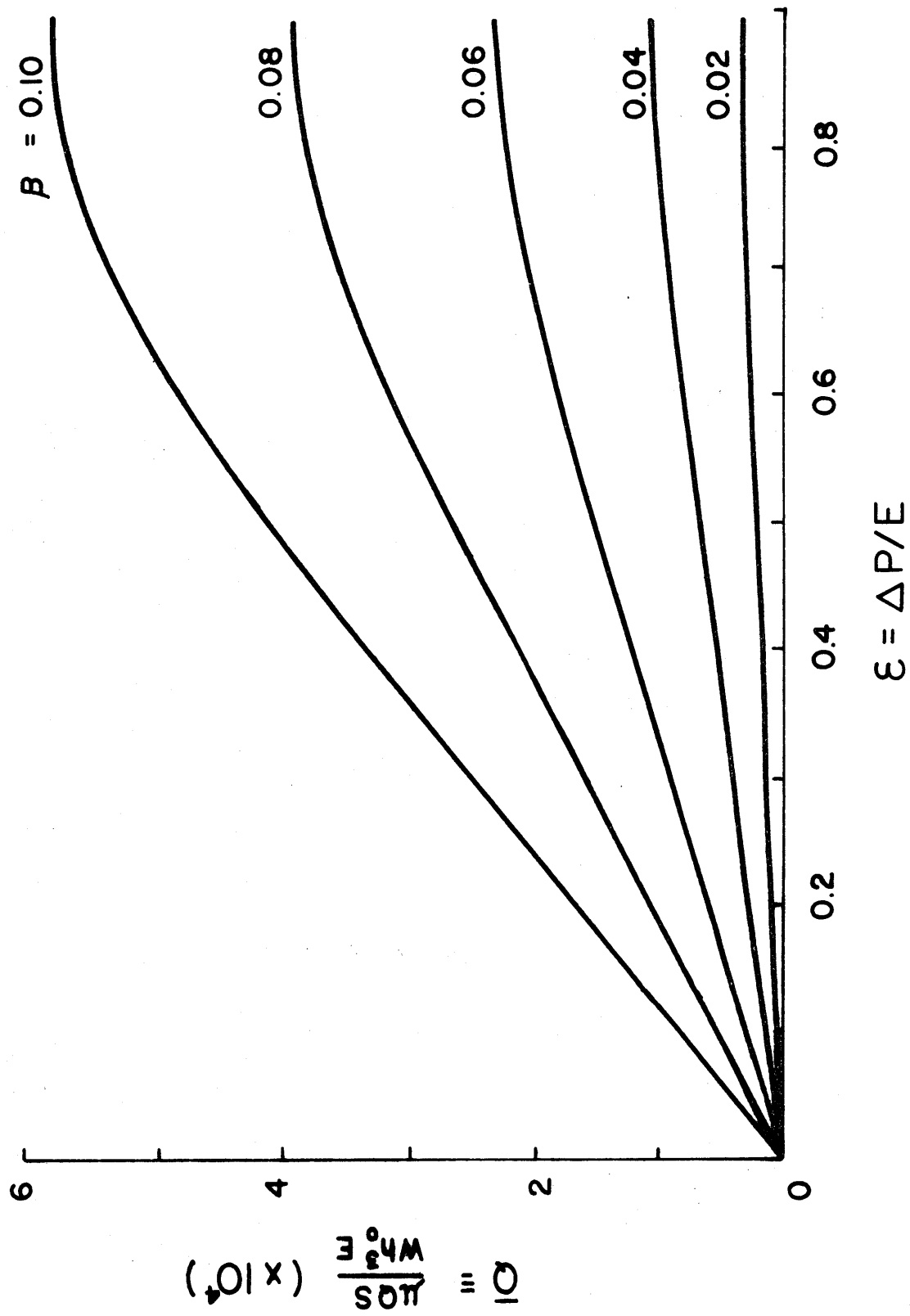

Figure 8

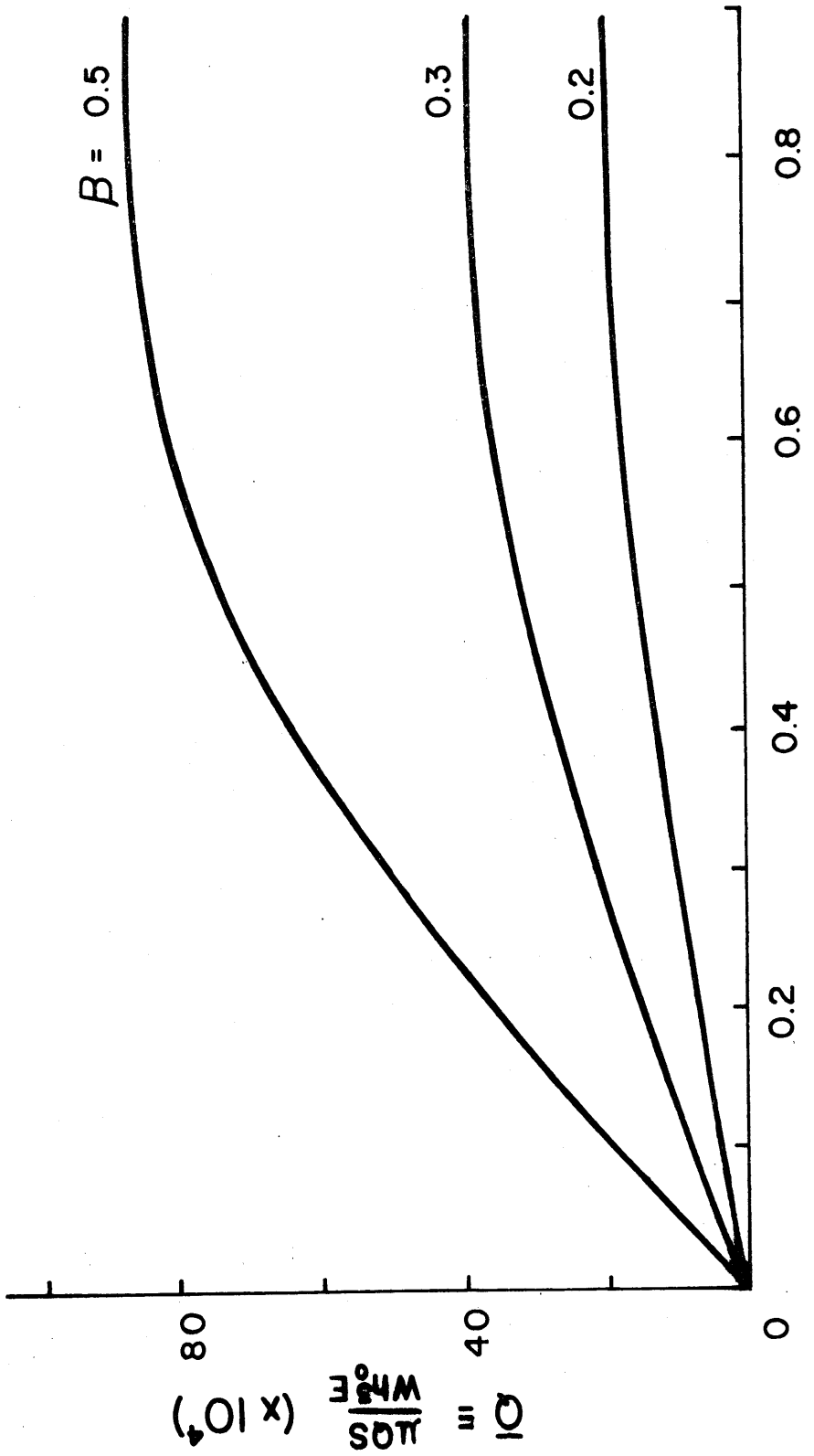

Figure 9

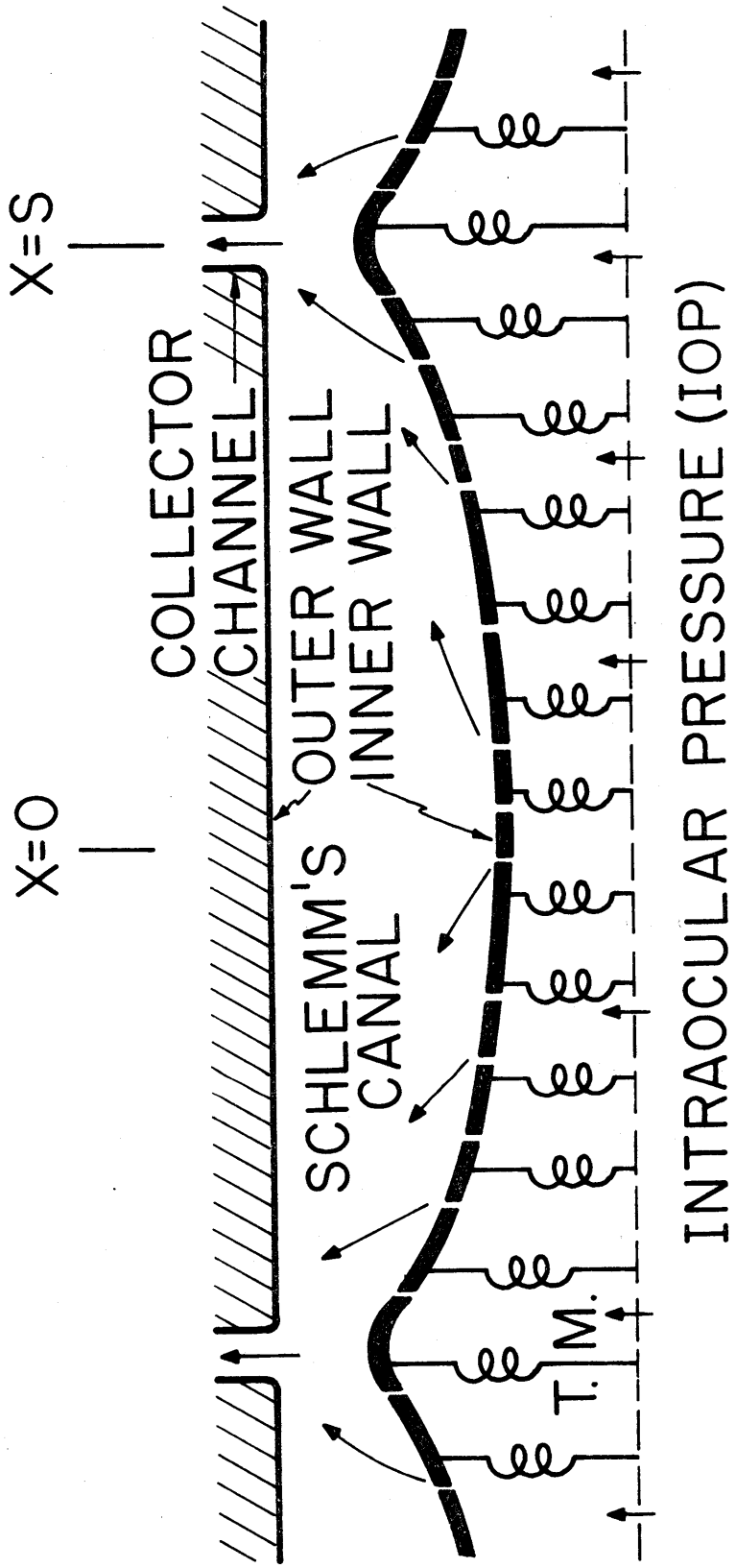
X=O
X=S
COLLECTOR CHANNEL
OUTER WALL
INNER WALL
SCHLEMM'S CANAL
T.M.
INTRAOCULAR PRESSURE (IOP)

Figure 10

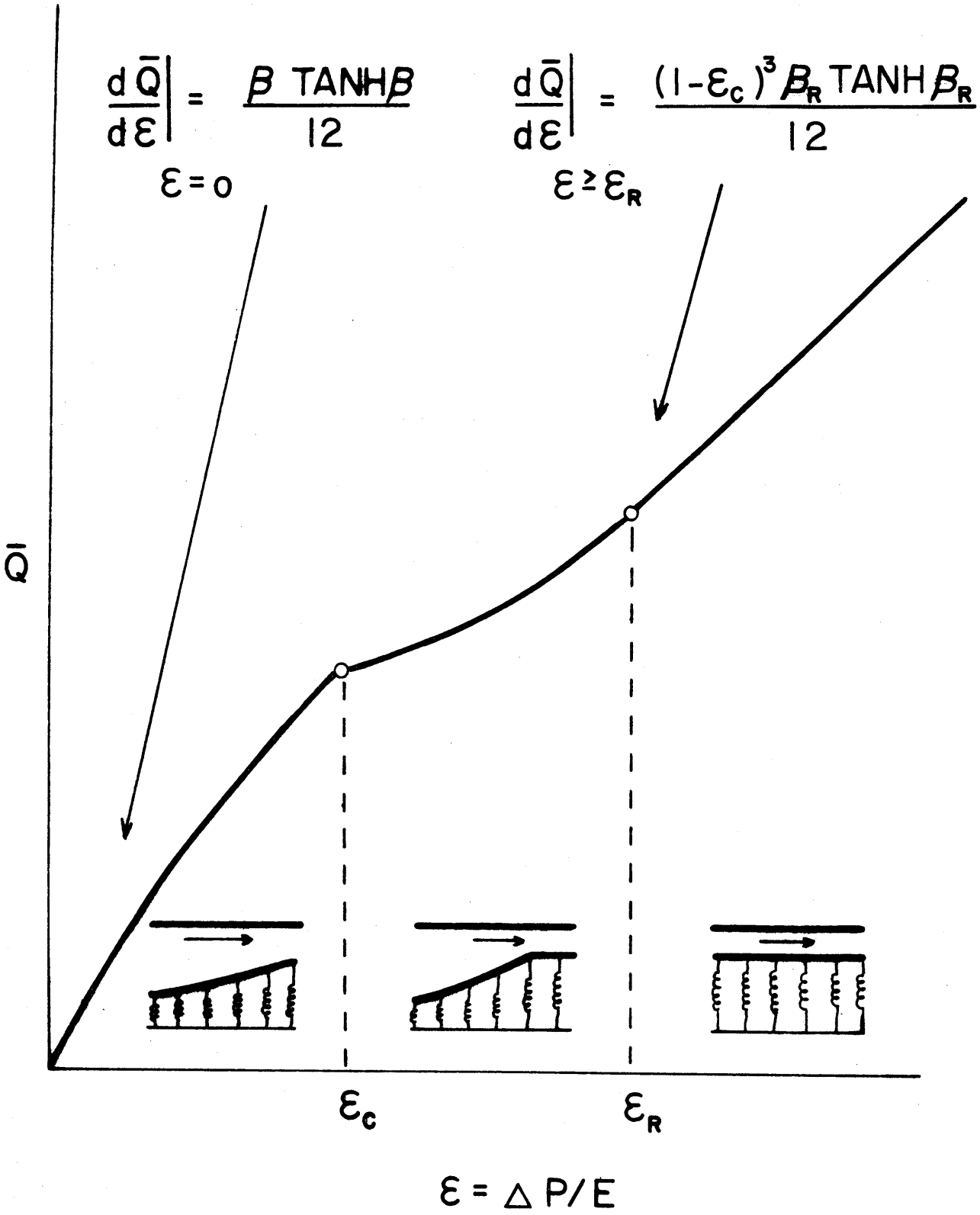
$\left|\frac{d\bar{Q}}{d\varepsilon}\right| = \frac{\beta \tanh\beta}{12}$
$\varepsilon = 0$
$\left|\frac{d\bar{Q}}{d\varepsilon}\right| = \frac{(1-\varepsilon_c)^3 \beta_R \tanh\beta_R}{12}$
$\varepsilon \geq \varepsilon_R$
$\bar{Q}$
ε_c
ε_R
$\varepsilon = \Delta P/E$

Figure 11

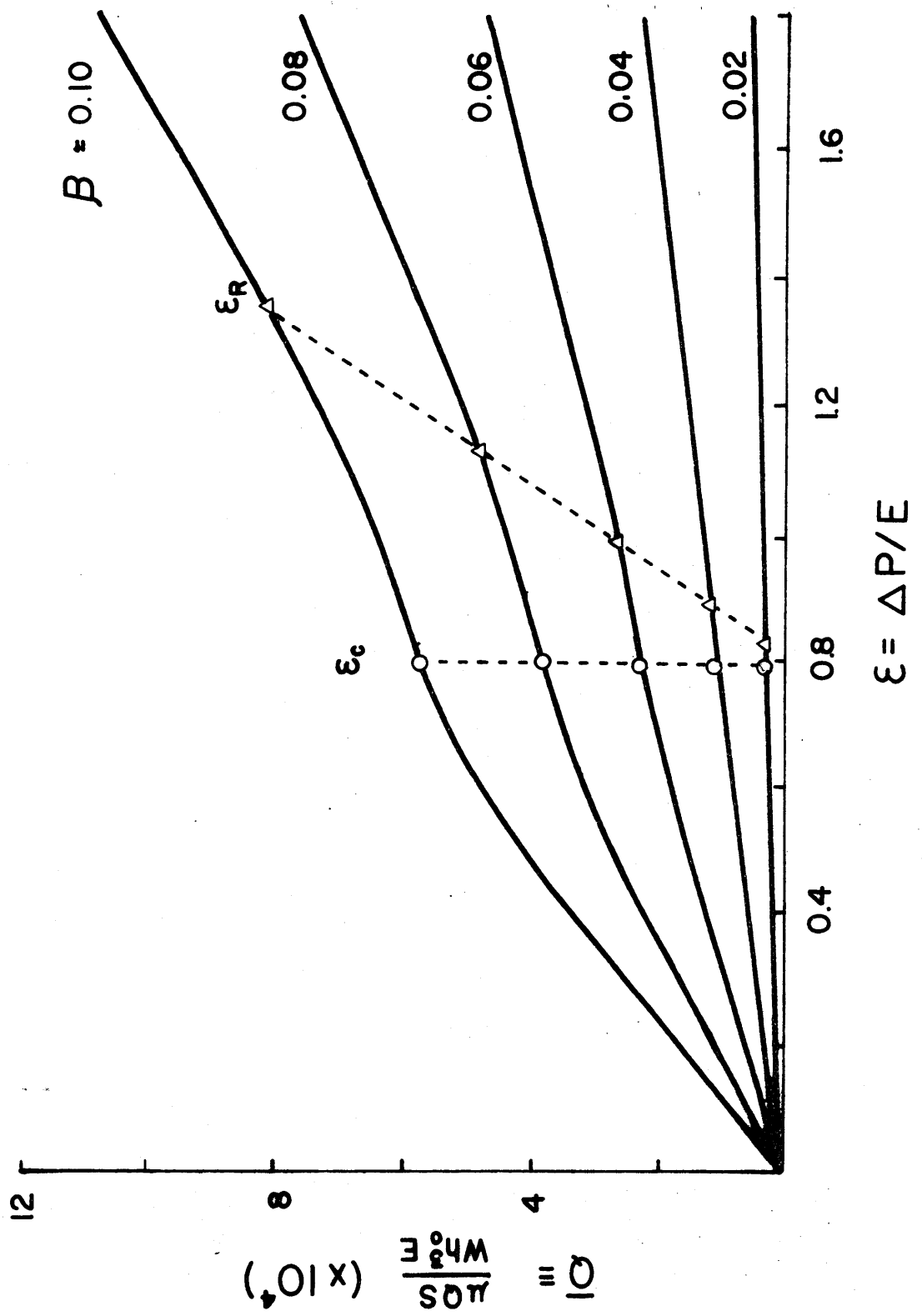
β = 0.10
0.08
0.06
0.04
0.02
ε_R
ε_c
12
8
4
0.4
0.8
1.2
1.6
$\varepsilon = \Delta P/E$
$\bar{Q} \equiv \frac{\mu_0 S}{W h_0^2 E}$ (x 10⁴)

Figure 12

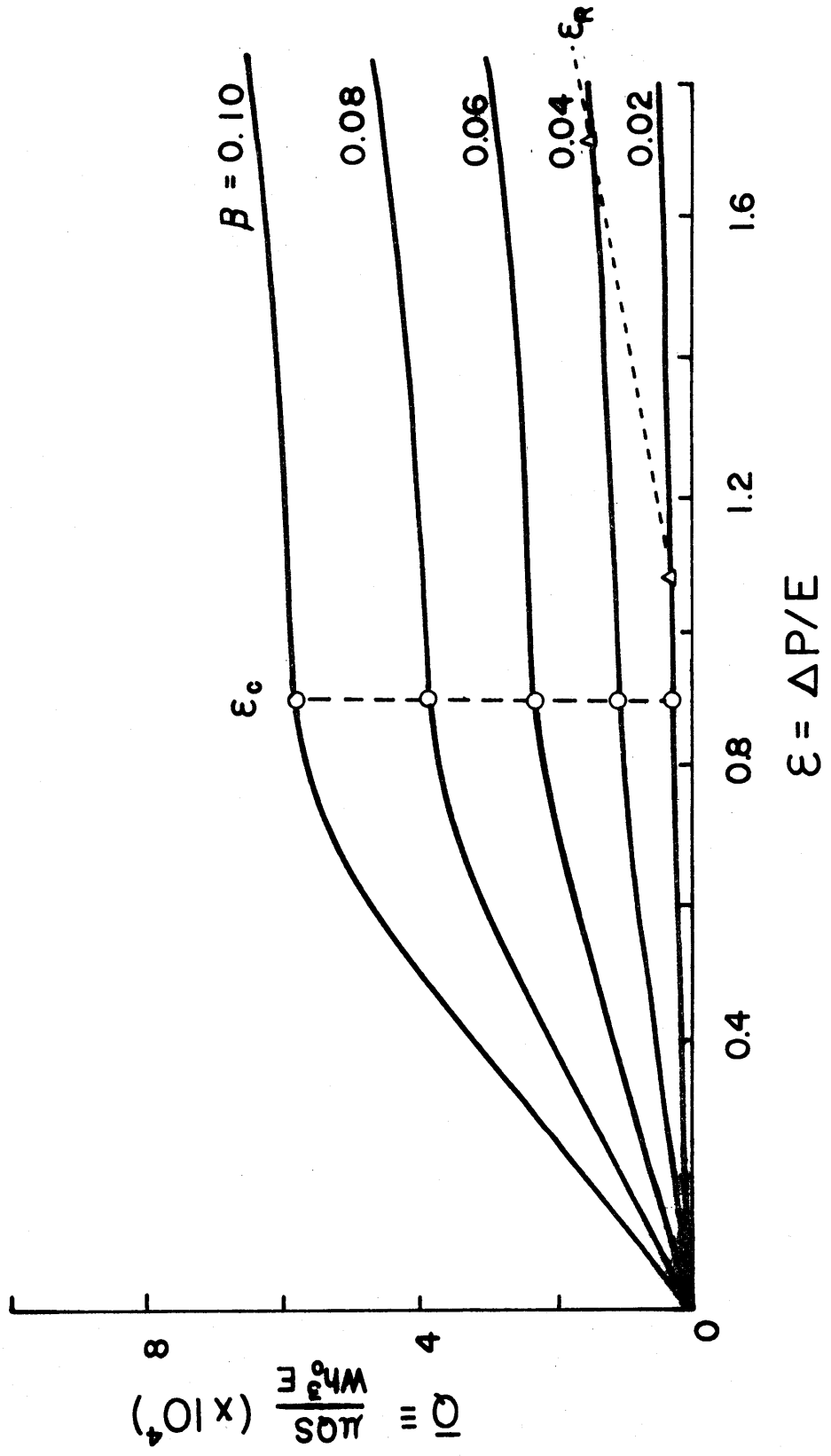
$\Omega = \frac{\mu_0 S}{w h_0^3 E}$ (x 10⁴)
8
4
0
0.4
0.8
1.2
1.6
ε = ΔP/E
β = 0.10
0.08
0.06
0.04
0.02
ε_c
ε_R

Figure 13

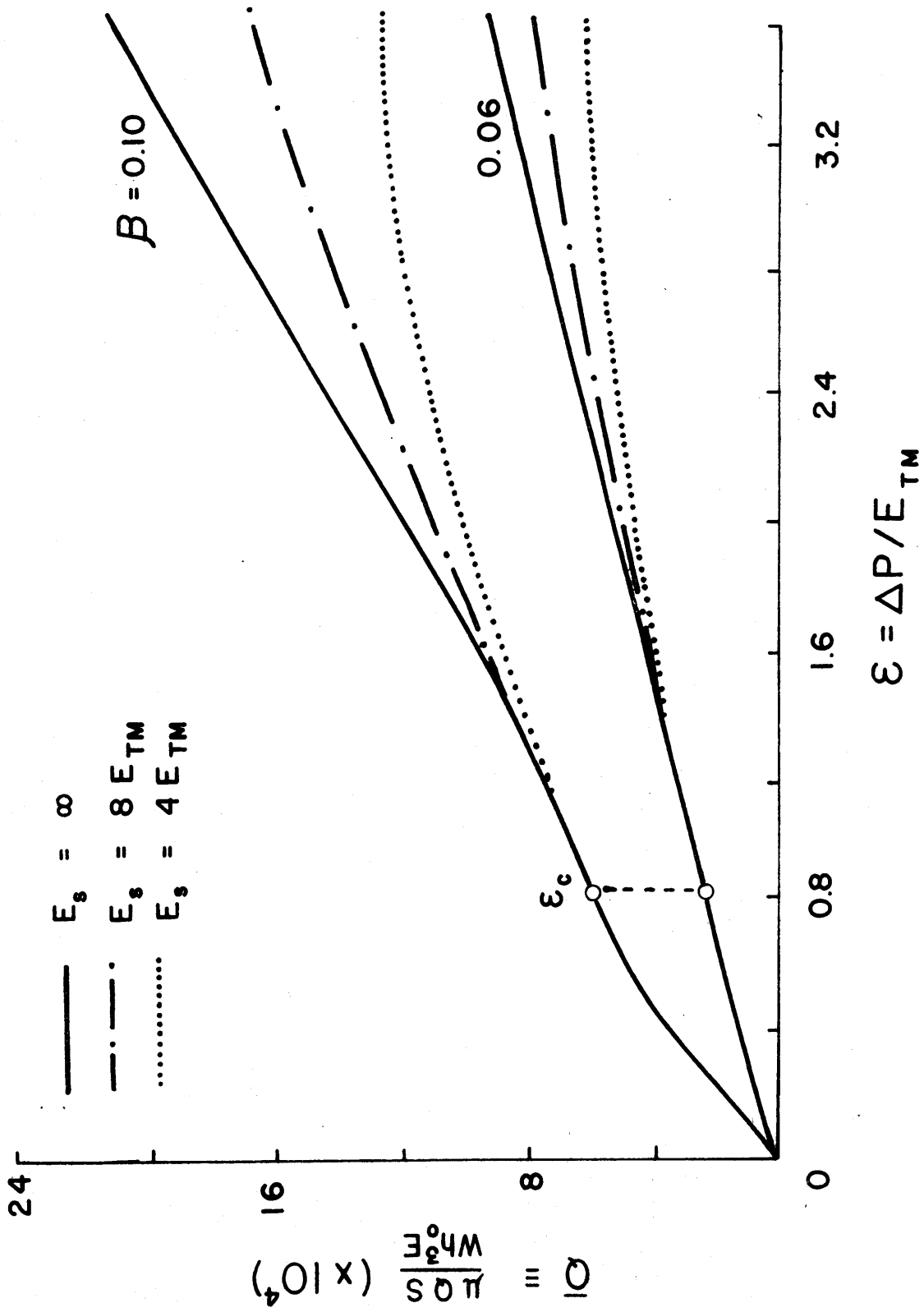
$\beta = 0.10$
0.06
$E_s = \infty$
$E_s = 8\,E_{TM}$
$E_s = 4\,E_{TM}$
ε_c
$Q \equiv \frac{\mu_0 S}{w h_0^3 E}$ $(\times 10^4)$
24
16
8
0
0.8
1.6
2.4
3.2
$\varepsilon = \Delta P / E_{TM}$

Figure 14

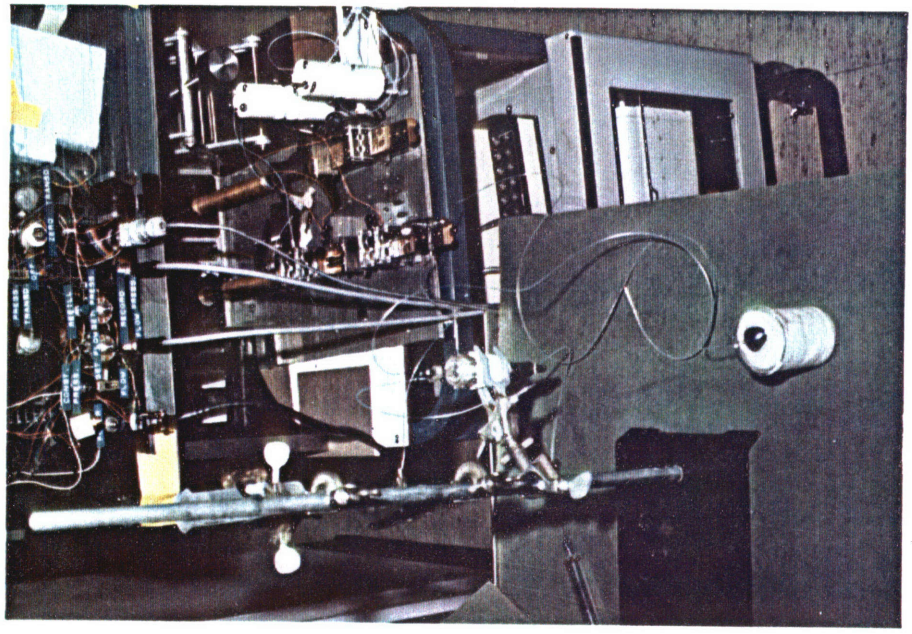

Figure 15b

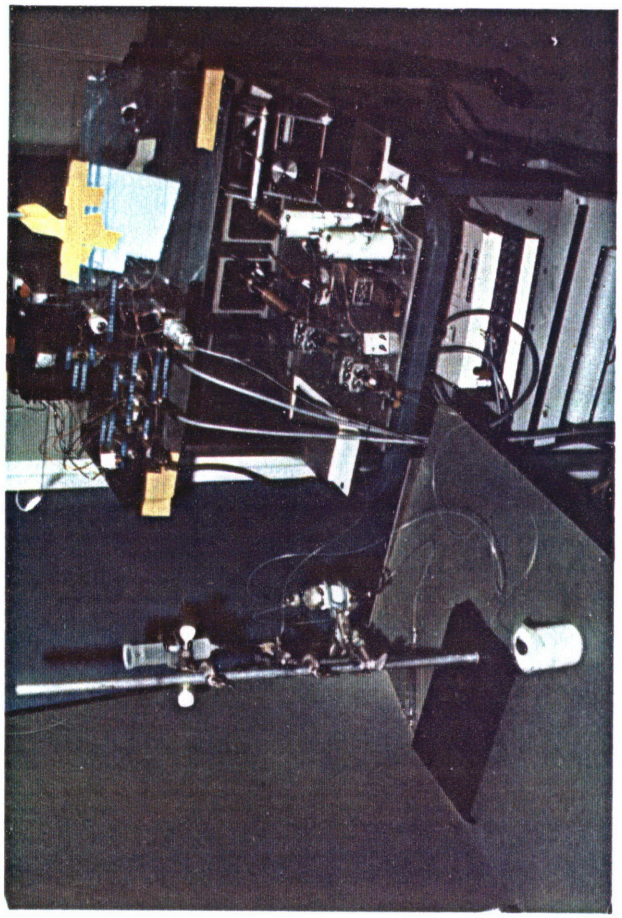

Figure 15a

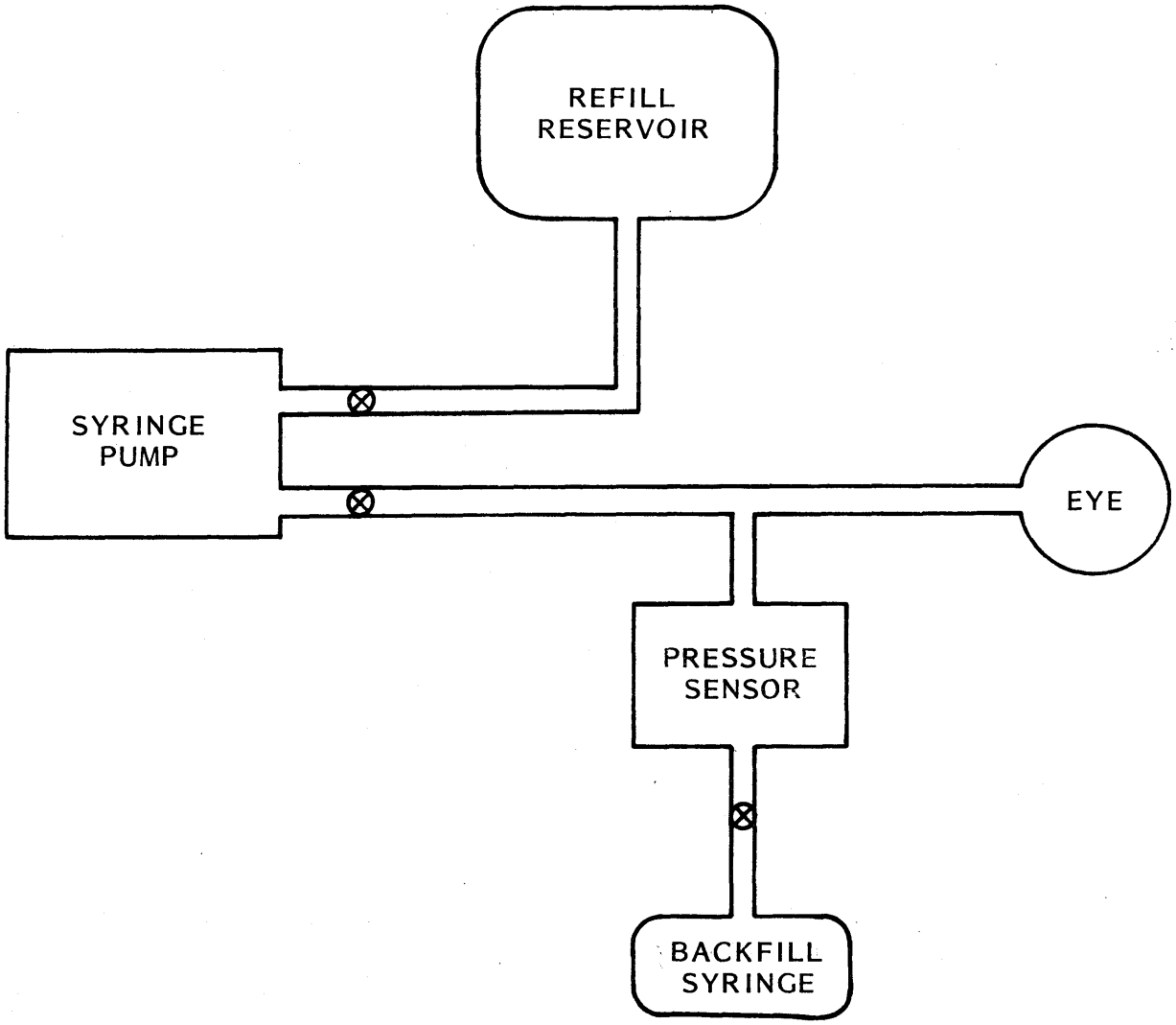
REFILL
RESERVOIR
SYRINGE
PUMP
EYE
PRESSURE
SENSOR
BACKFILL
SYRINGE

Figure 16

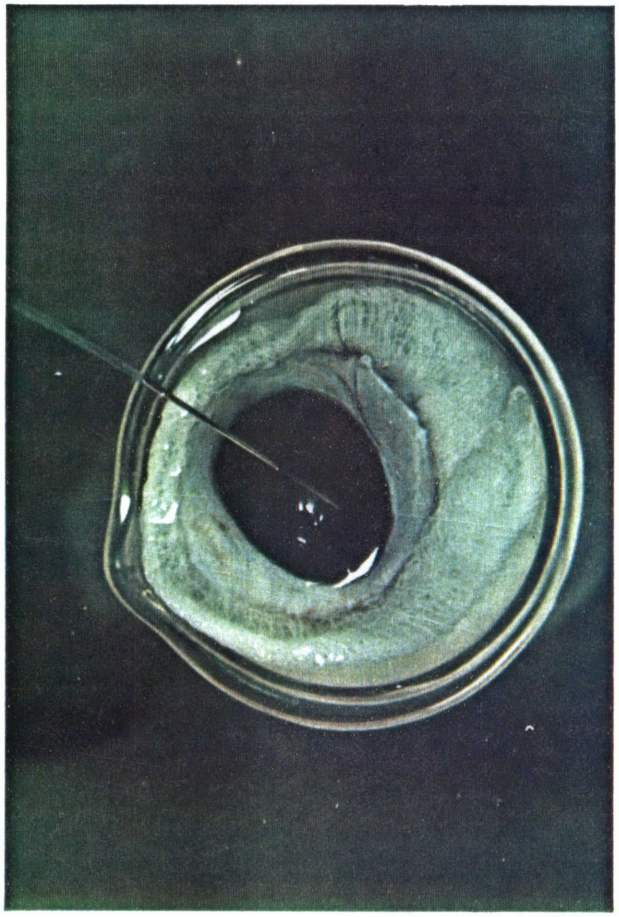

Figure 17b

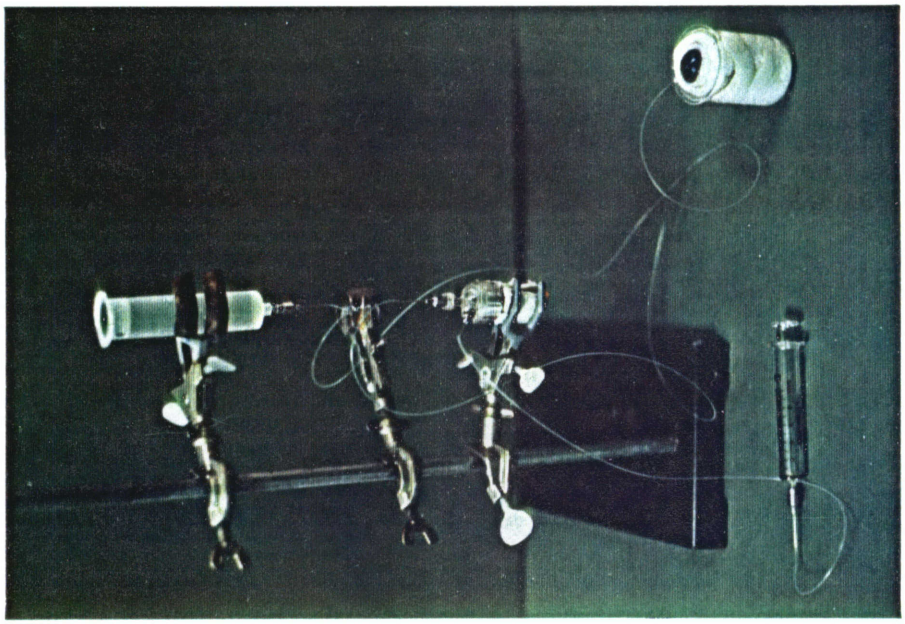

Figure 17a

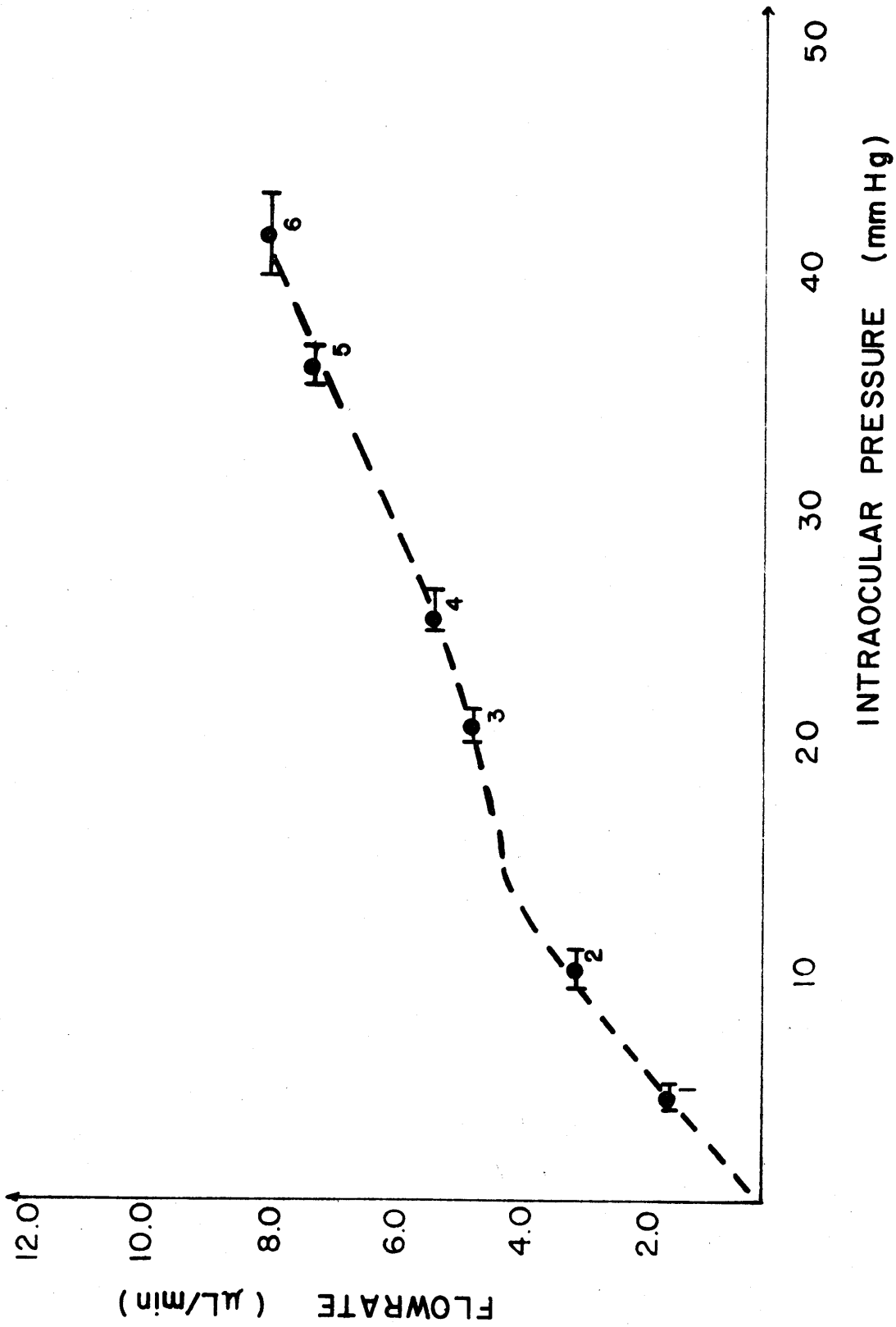
FLOWRATE (μL/min)
12.0
10.0
8.0
6.0
4.0
2.0
10
20
30
40
50
INTRAOCULAR PRESSURE (mmHg)
1
2
3
4
5
6

Figure 18

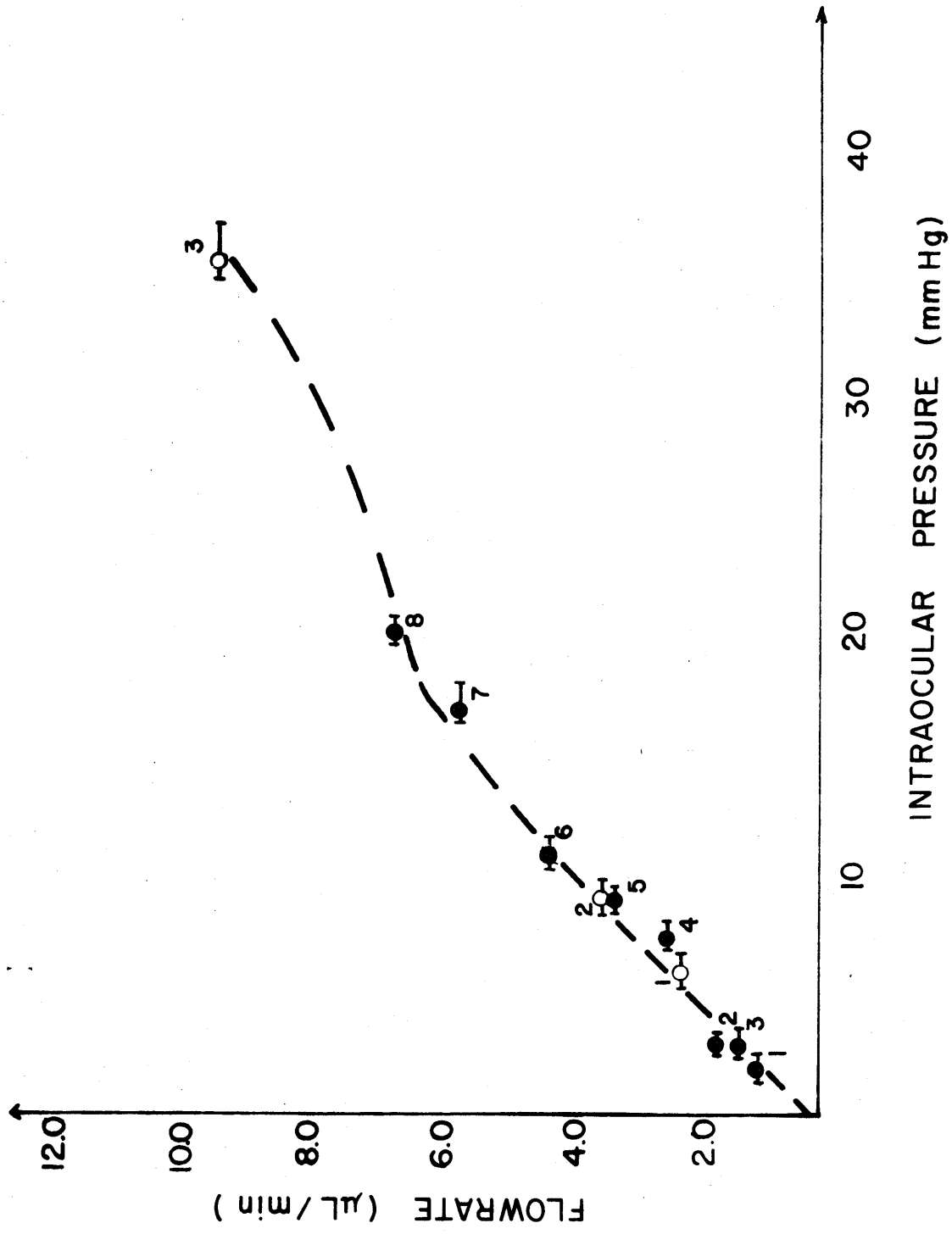
FLOWRATE (μL/min)
12.0
10.0
8.0
6.0
4.0
2.0
10
20
30
40
INTRAOCULAR PRESSURE (mm Hg)

Figure 19

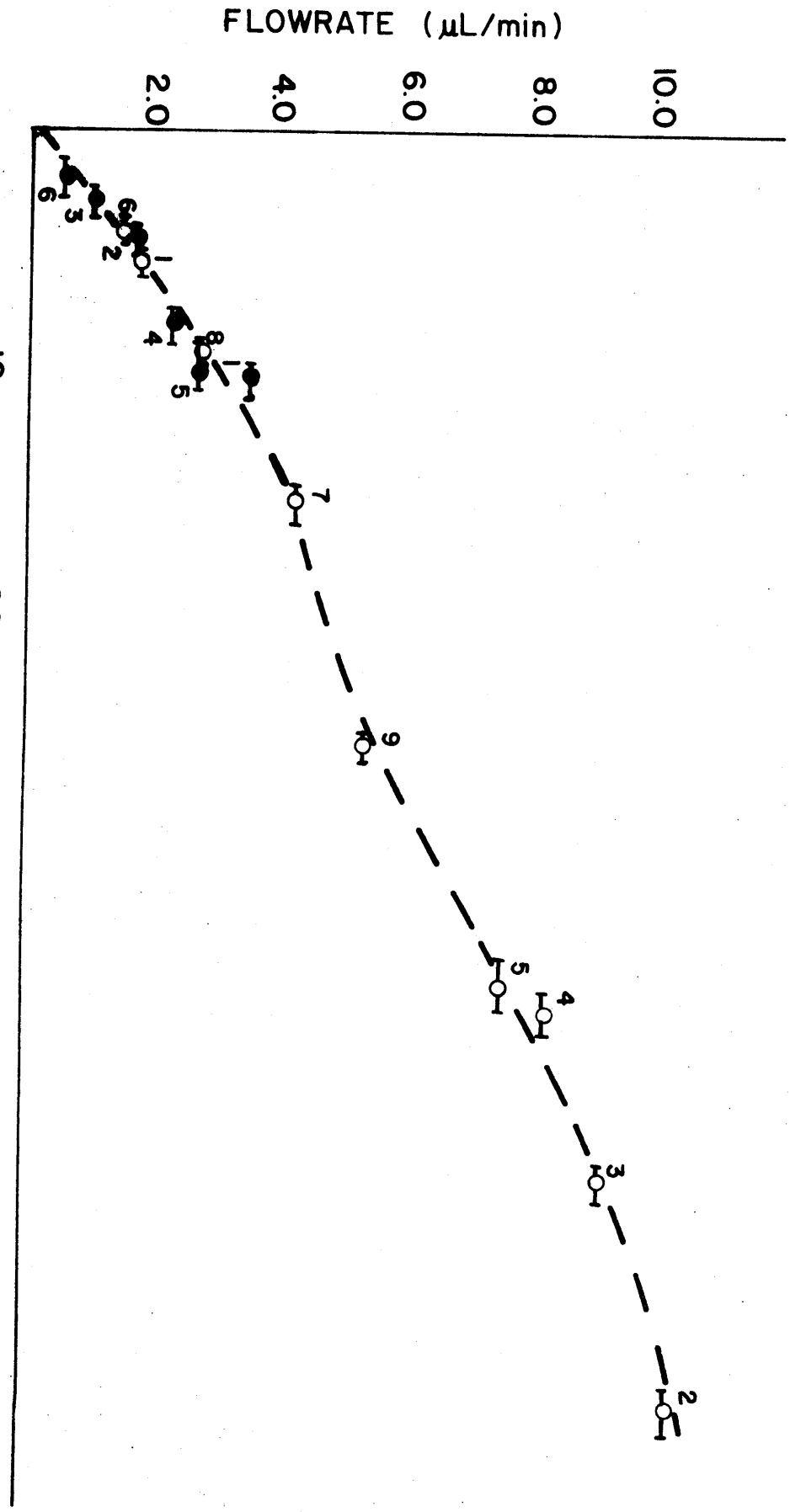
FLOWRATE (µL/min)
2.0
4.0
6.0
8.0
10.0
INTRAOCULAR PRESSURE (mm Hg)
10
20
30
40
50

Figure 20